Draft version August 5, 2019
Typeset using LaTeX **twocolumn** style in AASTeX61



# CONSTRAINTS ON THE PHYSICAL PROPERTIES OF TYPE IA SUPERNOVAE FROM PHOTOMETRY

R. Könyves-Tóth,[1] J. Vinkó,[1,2] A. Ordasi,[1] K. Sárneczky,[1] A. Bódi,[1,3] B. Cseh,[1] G. Csörnyei,[1] Z. Dencs,[1] O. Hanyecz,[1] B. Ignácz,[1] Cs. Kalup,[1] L. Kriskovics,[1] A. Pál,[1] B. Seli,[1] Á. Sódor,[1] R. Szakáts,[1] P. Székely,[4] E. Varga-Verebélyi,[1] K. Vida,[1] and G. Zsidi[1]

[1] *Konkoly Observatory, MTA CSFK, Konkoly-Thege M. ut 15-17, Budapest, Hungary*
[2] *Department of Optics and Quantum Electronics, University of Szeged, Hungary*
[3] *MTA CSFK Lendület Near-Field Cosmology Research Group*
[4] *Department of Experimental Physics,University of Szeged, Dóm tér 9., Szeged, Hungary*

## ABSTRACT

We present a photometric study of 17 Type Ia supernovae (SNe) based on multi-color (Bessell $BVR_CI_C$) data taken at Piszkéstető mountain station of Konkoly Observatory, Hungary between 2016 and 2018. We analyze the light curves (LCs) using the publicly available LC-fitter `SNooPy2` to derive distance and reddening information. The bolometric LCs are fit with a radiation-diffusion Arnett-model to get constraints on the physical parameters of the ejecta: the optical opacity, the ejected mass and the expansion velocity in particular. We also study the pre-maximum $(B-V)$ color evolution by comparing our data with standard delayed detonation and pulsational delayed detonation models, and show that the $^{56}$Ni masses of the models that fit the $(B-V)$ colors are consistent with those derived from the bolometric LC fitting. We find similar correlations between the ejecta parameters (e.g. ejecta mass, or $^{56}$Ni mass vs decline rate) as published recently by Scalzo et al. (2019).

*Keywords:* supenovae: general — supernovae: individual (Gaia16alq, SN 2016asf, SN 2016bln, SN 2016coj, SN 2016eoa, SN 2016ffh, SN 2016gcl, SN 2016gou, SN 2016ixb, SN 2017cts, SN 2017drh, SN 2017erp, SN 2017fgc, SN 2017fms, SN 2017hjy, SN 2017igf, SN 2018oh)

konyvestoth.reka@csfk.mta.hu

## 1. INTRODUCTION

Type Ia supernovae (SNe) are especially important objects for measuring extragalactic distances as their peak absolute magnitudes can be inferred via fitting their observed, multi-color LCs. Normal SN Ia events obey the empirical Phillips-relation (Pskovskii 1977; Phillips 1993), which states that the LCs of intrinsically fainter objects decline faster than those of brighter ones. The decline rate is often parametrized by $\Delta m_{15}$, i.e. the magnitude difference between the peak and the one measured at 15 days after maximum in a given (often the $B$) band. For example, the earlier version of the `SNooPy` code (Burns et al. 2011) applied $\Delta m_{15}$ as a fitting parameter for the decline rate. In the new version of `SNooPy` (Burns et al. 2014, 2018) a new parameter ($s_{BV}$) that measures the time difference between the maxima of the $B$-band light curve and the $B-V$ color curve, was introduced. Other parametrizations also exist: for example the `SALT2` code (Guy et al. 2007, 2010; Betoule et al. 2014) applies the $x_1$ (stretch) parameter, while `MLCS2k2` (Riess et al. 1998; Jha et al. 1999, 2007) uses $\Delta$. All of them are based on the same Phillips-relation, thus, $\Delta m_{15}$, $s_{BV}$, $x_1$ or $\Delta$ are related to each other.

Studying SNe Ia opens a door for constraining the Hubble-parameter $H_0$ (Riess et al. 2012, 2016; Dhawan et al. 2018a) by getting accurate distances to their host galaxies. Such absolute distances are the quintessential cornerstones of the cosmic distance ladder. Via constraining $H_0$, SNe Ia play a major role in investigating the expansion of the Universe (Riess et al. 1998; Perlmutter et al. 1999; Astier et al. 2006; Riess et al. 2007; Wood-Vasey et al. 2007; Kessler et al. 2009; Guy et al. 2010; Conley et al. 2011; Betoule et al. 2014; Rest et al. 2014; Scolnic et al. 2014; Bengaly et al. 2015; Jones et al. 2015; Li et al. 2016; Zhang et al. 2017) and testing the most recent cosmological models (e.g. Benitez-Herrera et al. 2013; Betoule et al. 2014).

Even though they are extensively used to estimate distances, the improvement of the precision as well as the accuracy of the method is still a subject of recent studies (see e.g. Vinkó et al. 2018). In order to achieve the desired 1% accuracy, it is important to understand the physical properties of the progenitor system and the explosion mechanism better.

The actual progenitor that explodes as a SN Ia, as well as the explosion mechanism, is still an issue. There are two main proposed progenitor scenarios: single-degenerate (SD) (Whelan & Iben 1973) and double-degenerate (DD) (Iben & Tutukov 1984). The SD scenario presumes that a carbon-oxygen white dwarf (C/O WD) has a non-degenerate companion star, e.g. a red giant, which, after overflowing its Roche-lobe, transfers mass to the WD. When the WD approaches the Chandrasekhar mass, spontaneous fusion of C/O to $^{56}$Ni develops that quickly engulfs the whole WD, leading to a thermonuclear explosion.

The details on the onset and the progress of the C/O fusion is still debated, and many possible mechanisms have been proposed in the literature. The most successful one is the delayed detonation explosion (DDE) model, in which the burning starts as a deflagration, but later it turns into a detonation wave (Nomoto et al. 1984; Khokhlov 1991; Dessart et al. 2014; Maoz et al. 2014). A variant of that is the pulsational delayed detonation explosion (PDDE): during the initial deflagration phase the expansion of the WD expels some material from its outmost layers, which pulsates, expands and avoids burning. After that, the bound material falls back to the WD that leads to a subsequent detonation (Dessart et al. 2014).

There is a theoretical possibility for a sub-Chandrasekhar double-detonation scenario, where the WD accretes a thin layer of helium onto its surface, which is compressed by its own mass that leads to He-detonation This triggers the thermonuclear explosion of the underlying C/O WD (Woosley & Weaver 1994; Fink et al. 2010; Kromer et al. 2010; Sim et al. 2010, 2012).

In the DD scenario two WDs merge or collide that results in a subsequent explosion (Maoz et al. 2014; van Rossum et al. 2016).

It may be possible to distinguish between these scenarios e.g. by constraining the mass of the progenitor. Thus, the ejecta mass is an extremely important physical quantity, which can be inferred by fitting LC models to the observations.

The idea that the bolometric LC of SNe Ia can be used to infer the ejecta mass via a semi-analytical model, was introduced by Arnett (1982) and developed further by Jeffery (1999). Arnett (1982) showed that the ejecta mass correlates with the rise time to maximum light, provided the expansion velocity and the mean optical opacity of the ejecta are known. Later, Jeffery (1999) suggested the usage of the rate of the deviation of the observed LC from the rate of the Cobalt-decay during the early nebular phase (i.e. the transparency timescale, $t_\gamma$), which measures the leakage of $\gamma$-photons from the diluting ejecta. The advantage of using $t_\gamma$ for constraining the ejecta mass is that $t_\gamma$ is proportional to the gamma-ray opacity, which is much better known than the mean optical opacity. This technique was applied to real data by Stritzinger et al. (2006), Scalzo et al. (2014) and more recently by Scalzo et al.

(2019). The conclusion of all these studies was that most SNe Ia seem to have sub-Chandrasekhar mass ejecta, which was also confirmed recently by theoretical models (Dhawan et al. 2018b; Goldstein, & Kasen 2018; Wilk et al. 2018; Papadogiannakis et al. 2019).

The usage of the transparency timescale as a proxy for the ejecta mass has some caveats, though. $t_\gamma$ also depends on the characteristic velocity ($v_e$) of the expanding ejecta, which is not easy to constrain as it is related to the velocity of a layer deep inside the ejecta. Stritzinger et al. (2006), for example, assumed that $v_e$ is uniform for all SNe Ia (they adopted $v_e \sim 3000$ km s$^{-1}$), which may not be true in reality, because it is known that a diversity in expansion velocities exists for most SNe Ia (Wang et al. 2013). Another issue is the distribution of the radioactive $^{56}$Ni, encoded by the $q$ parameter by Jeffery (1999), which is usually taken from models ($q \sim 1/3$, given by the W7 model, is often assumed). These assumptions, although may not be too far from reality, might introduce some sort of systematic uncertainties in the inferred ejecta masses, which may be worth for further studies.

The main motivation of the present paper is to give constraints on the ejecta mass and some other physical parameters for a sample of 17 recent SNe Ia (Figure 1 and 2) observed from Piszkéstető station of Konkoly Observatory, Hungary. We generalize the prescription of inferring the ejecta masses by combining the LC rise time and the transparency timescale within the framework of the constant-density Arnett-model.

In the following we present the description of the photometric sample (Section 2), then we show the results from multi-color LC modeling (Section 3). We construct and fit the bolometric LCs in order to derive the ejecta mass, and other parameters such as the diffusion- and gamma-leakage timescales, the optical opacity and the expansion velocity.

In Section 4, we first discuss the early (de-reddened) $(B-V)_0$ color evolution, which might also provide some constraints on the explosion mechanism and the progenitor system (Hosseinzadeh et al. 2017; Miller et al. 2018; Stritzinger et al. 2018). There is a growing number of evidence for the appearance of blue excess light during the earliest phase of some SNe Ia (Marion et al. 2016; Hosseinzadeh et al. 2017; Dimitriadis et al. 2019; Li et al. 2018; Shappee et al. 2019; Stritzinger et al. 2018). At present the cause of this excess emission is debated, and a number of possible explanations were proposed recently (Hosseinzadeh et al. 2017; Miller et al. 2018; Stritzinger et al. 2018; Hosseinzadeh et al. 2017). These include

- SN shock cooling;
- interaction with a non-degenerate companion;
- presence of high velocity $^{56}$Ni in the outer layers of the ejecta;
- interaction with the circumstellar matter (CSM);
- differences in the composition or variable opacity.

Furthermore, we compare our measured $(B-V)_0$ colors with the predictions of various explosion models (Dessart et al. 2014), and examine the possible correlations between the derived physical parameters following Scalzo et al. (2014), Scalzo et al. (2019) and Khatami & Kasen (2018).

Finally Section 5 summarizes the results of this paper.

## 2. OBSERVATIONS

We obtained multi-band photometry for 17 bright Type Ia SNe from the Piszkéstető station of Konkoly Observatory, Hungary between 2016 and 2018. The selection criteria for the sample were as follows: i) accessibility from the site (i.e. declination above $-15$ degree), ii) sufficiently early (pre-maximum) discovery, iii) ability for follow-up beyond $t \sim +40$ days after maximum, and iv) low redshift ($z \lesssim 0.05$).

All data were taken with the 60/90 cm Schmidt-telescope equipped with a $4096 \times 4096$ FLI CCD and Bessell $BVRI$ filters, thus, providing a homogeneous, high signal-to-noise data sample of nearby SNe Ia.

Data reduction and photometry was done the same way as described in Vinkó et al. (2018). The raw data were reduced using IRAF[1] (Image Reduction and Analysis Facility) by completing bias, dark and flatfield corrections. Geometric registration of the sky frames was made in two steps. First, we used `SExtractor` (Bertin, E. & Arnouts, S. 1996) for identifying point sources on each frame. Second, the `imwcs` routine from the `wcstools`[2] package was applied to assign R.A. and Dec. coordinates to pixels on the CCD frames.

Photometry on each SN and several other local comparison stars was made via PSF-fitting. Note that due to the strong, variable background from the host galaxy, image subtraction was unavoidable in the case of SN 2016coj, 2016gcl, 2016ixb, 2017drh and 2017hjy. For subtraction we used template frames taken with the same telescope and instrumental setup more than 1 year after the discovery of the SN. In these cases the photometry of the comparison stars was computed on the unsubtracted frames, while it was done on the host-subtracted frames for the SN. Particular attention was

[1] http://iraf.noao.edu
[2] http://tdc-www.harvard.edu/wcstools/

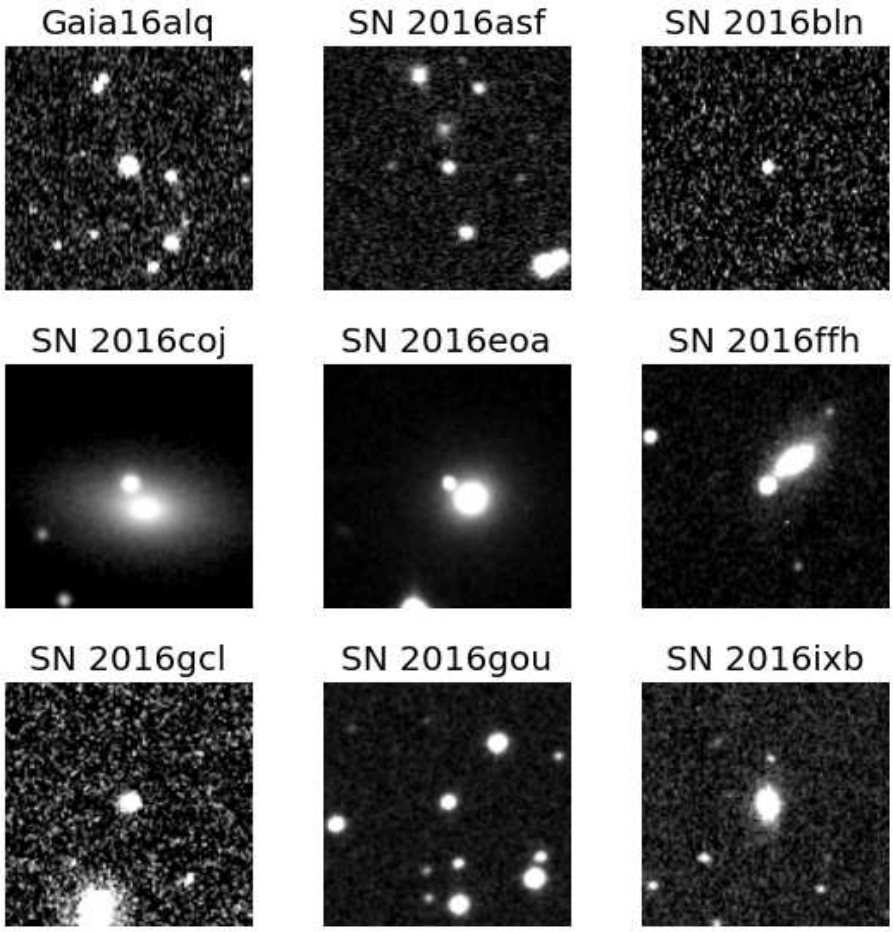


**Figure 1.** Images of the program SNe observed in 2016. The size of each subframe is $1.7 \times 1.7$ arcmin$^2$. The supernova is the central object, while North is up and East is to the left.

paid to keep the flux zero point of the subtracted frame the same as that of the unsubtracted one, thus, getting consistent photometry from both frames. Simple PSF fitting gave acceptable results in the case of the other SNe that suffered less severe contamination from their hosts.

The magnitudes of the local comparison stars were determined from their PS1-photometry[3] after transforming the PS1 $g_P, r_P, i_P$ magnitudes to the Johnson-Cousins $BVRI$ system. The zero points of the standard transformation were tied to these magnitudes.

The basic data of the observed SNe are collected in Table 1. Plots of the $V$-band sub-frames centered on the SNe are shown in Fig 1 and 2. After acceptance, all photometric data will be made available via the *Open Supernova Catalog*[4].

## 3. ANALYSIS

### 3.1. *Multi-color light curve modeling*

To fit and analyze the observed LCs, we used the `SNooPy2`[5] (Burns et al. 2011, 2014) LC fitter, which is based on the Phillips-relation (Phillips 1993). It can be categorized as a "distance calculator" (Conley et al. 2008), since it provides the absolute distance as a fitting parameter.

We applied both the EBV-model that fits the template LCs by Prieto et al. (2006) to the data in $BVRI$ filters, and the EBV2-model that is based on the $uBVgriYJH$

[3] `https://archive.stsci.edu/panstarrs/`

[4] `https://sne.space`

[5] http://csp.obs.carnegiescience.edu/data/snpy/snpy

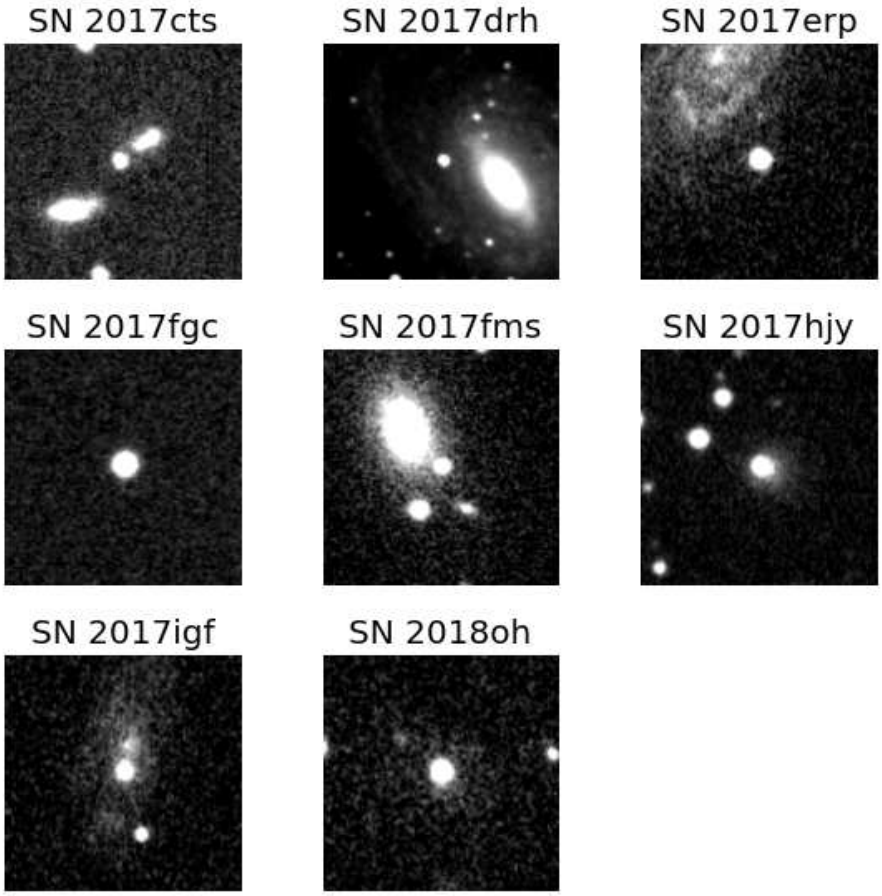


**Figure 2.** The same as Figure 1 but for the SNe observed in 2017 and 2018.

light curves by Burns et al. (2011). Both of these models relate the distance modulus of a normal SN Ia to its decline rate and color as

$$m_X(\varphi) = T_Y + M_Y + \mu_0 + K_{XY} + \\ + R_X \cdot E(B-V)_{MW} + R_Y \cdot E(B-V)_{host}, \quad (1)$$

where X and Y represent the filter of the template LC and the observed data, $m_X(\varphi)$ is the observed LC in filter X, $T_Y(\varphi, p)$ is the template LC as a function of time, $p$ is a generalized decline rate parameter ($p = \Delta m_{15}$ or $p = s_{BV}$ in the EBV and EBV2 models, respectively), $\mu_0$ is the reddening-free distance modulus in magnitudes, $E(B-V)$ is the color excess due to interstellar extinction either in the Milky Way (MW), or in the host galaxy, $R_{X,Y}$ are the reddening slopes in filter X or Y and $K_{XY}(t, z)$ is the cross-band K-correction that matches the observed broad-band magnitudes of a redshifted SN taken with filter X to a template SN LC taken in filter Y. Since our SNe have very low redshifts, K-corrections are often negligible compared to the observational uncertainties (see Table 1).

The motivation behind using the EBV2 model, despite the difference between the photometric system of its LC templates and our data, is that the EBV2 model allows the fitting of the $s_{BV}$ decline rate parameter, which is more suitable for describing fast-decliner (91bg-like) SNe Ia than the canonical $\Delta m_{15}$ (Burns et al. 2014)[6].

We fit the observed $BVRI$ LCs, adopting $R_V = 3.1$ for the reddening slope, with $\chi^2$-minimization using the built-in MCMC routine in `SNooPy2`. The inferred parameters are the following:

- $E(B-V)_{host}$ : interstellar extinction of the host galaxy (in magnitude);
- $T_{max}$ : moment of the maximum light in the B-band (in MJD);

[6] We thank the referee for this suggestion.

**Table 1.** Basic data of the observed SNe

| SN name | Type | R.A. | Dec. | Host galaxy | $z$ | Discovery | Ref. |
|---|---|---|---|---|---|---|---|
| Gaia16alq | Ia-norm | 18:12:29.36 | +31:16:47.32 | PSO J181229.441+311647.834 | 0.023 | 2016-04-21 | a |
| SN 2016asf | Ia-norm | 06:50:36.73 | +31:06:45.36 | KUG 0647+311 | 0.021 | 2016-03-06 | b |
| SN 2016bln | Ia-91T | 13:34:45.49 | +13:51:14.30 | NGC 5221 | 0.0235 | 2016-04-04 | c |
| SN 2016coj | Ia-norm | 12:08:06.80 | +65:10:38.24 | NGC 4125 | 0.005 | 2016-05-28 | d |
| SN 2016eoa | Ia-91bg | 00:21:23.10 | +22:26:08.30 | NGC 0083 | 0.021 | 2016-08-02 | e |
| SN 2016ffh | Ia-norm | 15:11:49.48 | +46:15:03.22 | MCG +08-28-006 | 0.018 | 2016-08-17 | f |
| SN 2016gcl | Ia-91T | 23:37:56.62 | +27:16:37.73 | AGC 331536 | 0.028 | 2016-09-08 | g |
| SN 2016gou | Ia-norm | 18:08:06.50 | +25:24:31.32 | PSO J180806.461+252431.916 | 0.016 | 2016-09-22 | h |
| SN 2016ixb | Ia-91bg | 04:54:00.04 | +01:57:46.62 | NPM1G +01.0158 | 0.028343 | 2016-12-17 | i |
| SN 2017cts | Ia-norm | 17:03:11.76 | +61:27:26.06 | CGCG 299-048 | 0.02 | 2017-04-02 | j |
| SN 2017drh | Ia-norm | 17:32:26.05 | +07:03:47.52 | NGC 6384 | 0.005554 | 2017-05-03 | k |
| SN 2017erp | Ia-norm | 15:09:14.81 | -11:20:03.20 | NGC 5861 | 0.0062 | 2017-06-13 | l |
| SN 2017fgc | Ia-norm | 01:20:14.44 | +03:24:09.96 | NGC 0474 | 0.008 | 2017-07-11 | m |
| SN 2017fms | Ia-91bg | 21:20:14.60 | -04:52:51.30 | IC 1371 | 0.031 | 2017-07-17 | n |
| SN 2017hjy | Ia-norm | 02:36:02.56 | +43:28:19.51 | PSO J023602.146+432817.771 | 0.007 | 2017-10-14 | o |
| SN 2017igf | Ia-91bg | 11:42:49.85 | +77:22:12.94 | NGC 3901 | 0.006 | 2017-11-18 | p |
| SN 2018oh | Ia-norm | 09:06:39.54 | +19:20:17.77 | UGC 04780 | 0.012 | 2018-02-04 | q |

NOTE—a: Piascik, & Steele (2016); b: Cruz et al. (2016); c: Miller et al. (2016); d: Zheng et al. (2017); e: Gagliano et al. (2016); f: Tonry et al. (2016); g: Brown (2016); h: Tonry et al. (2016); i: Stanek (2016); j: Brimacombe et al. (2017); k: Valenti et al. (2017); l: Itagaki (2017); m: Sand et al. (2017); n: Gagliano et al. (2017); o: Tonry et al. (2017); p: Stanek (2017); q: Stanek (2018)

- $\mu_0$ : extinction-free distance modulus (in magnitude);
- $s_{BV}$: decline rate parameter in the EBV2 model
- $\Delta m_{15}$ : decline rate parameter in the EBV model (in magnitude).

We also attempted to include $R_V$ as a fitting parameter, but the results were close the original $R_V = 3.1$ value, indicating that our photometry is not suitable for constraining this parameter. This is not surprising, given the lack of UV- or NIR-data in our sample.

Note that since the EBV2 model is based on a different photometric system than our Johnson-Cousins $BVRI$ data, the inferred best-fit values for $E(B-V)$ and $\mu_0$ are expected to be slightly different from those obtained from the EBV model that is based on $BVRI$ data. After comparing the best-fit parameters taken from both models, it is found that the $E(B-V)$ values are consistent with each other within $1\sigma$, while there is a systematic shift of $\mu_0(EBV) - \mu_0(EBV2) \sim 0.1$ mag between the distance moduli. For consistency, we decided to adopt the $E(B-V)$ and $\mu_0$ parameters from the EBV2 model as final, but added $\sim 0.1$ mag systematic uncertainty to the distance modulus (corresponding to $\sim 5$ percent relative error in the distances).

The final best-fit parameters are shown in Table 2. The reported errors include the systematic uncertainties of the template vectors as given by `SNooPy2`.

Plots of the observed LCs and their best-fit `SNooPy2` templates can be found in the Appendix (Fig. 11). The overall fitting quality is good; most of the reduced $\chi^2$ values (column 8 in Table 2) are in between 1 and 2, and the highest $\chi^2 \sim 6.6$ is that of SN 2016gou. As it can be seen in Fig. 11, the fit to SN 2016gou around maximum is very good, and the relatively high $\chi^2$ value is likely caused by the scattering in the last few data points after +40 days.

As seen in Table 2, the host reddening of SN 2017drh turned out to be extremely high ($E(B-V)_{host} \sim 1.4$ mag) compared to the rest of the sample. Since this may add an extra uncertainty in the derived distance and other parameters, SN 2017drh was excluded from the sample and was not analyzed further.

### 3.2. *Construction of the bolometric light curve*

While constructing the bolometric LCs we followed the same procedure as applied recently by Li et al.

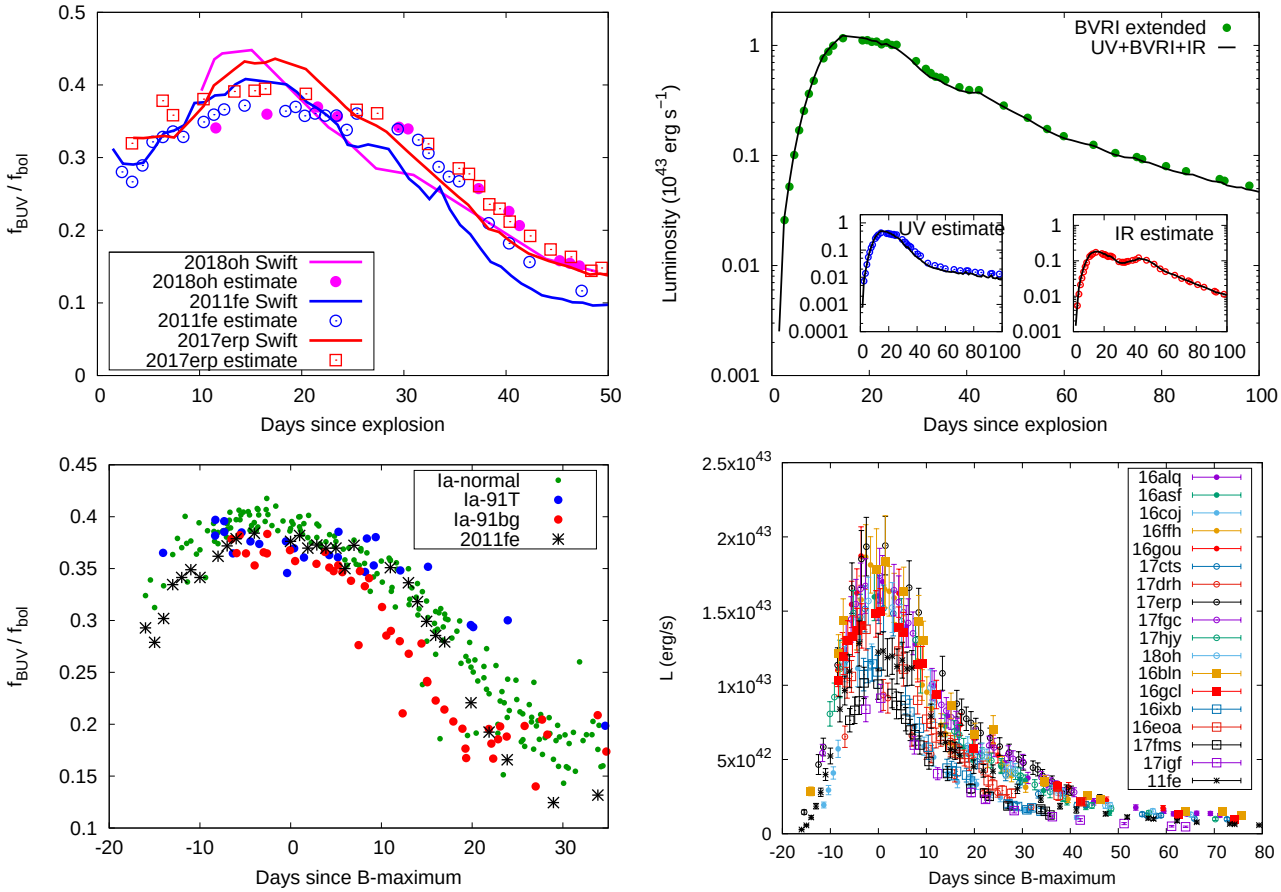


**Figure 3.** Top left panel: the ratio of BUV flux to the total bolometric flux as a function of time since explosion for SN 2018oh (magenta), SN 2011fe (blue) and SN 2017erp (red). Data obtained by direct integration of *Swift* fluxes are plotted with lines, while the symbols correspond to data estimated from $BVRI$ observations (see text). Top right panel: Comparison of the pseudo-bolometric LCs of SN 2011fe derived from the extrapolated $BVRI$ SED (symbols) and by direct integration of the observed UV + optical + NIR data (black line). The two insets show the UV and the IR contributions separately. Bottom left panel: the same as the top left panel but for the whole observed sample. Colors code the different SN subtypes as indicated in the legend. Bottom right panel: the derived pseudo-bolometric light curves for the sample SNe.

(2018) for SN 2018oh. Briefly, after correcting for extinction within the Milky Way and the host galaxy (Table 1 and 2), the observed $BVRI$ magnitudes were converted to physical fluxes via the calibration of Bessell et al. (1998). Then, the fluxes were integrated against wavelength via the trapezoidal rule. The missing UV- and IR bands are estimated by extrapolations in the following way.

In the UV regime the flux was assumed to decrease linearly between 2000 Å and $\lambda_B$, and the UV-contribution was estimated from the extinction-corrected $B$-band flux $f_B$ as $f_{bol}^{UV} = 0.5 f_B(\lambda_B - 2000)$.

In the IR, a Rayleigh-Jeans tail was fit to the corrected $I$-band flux $f_I$ and integrated between $\lambda_I$ and infinity to get $f_{bol}^{IR} = 1.3 f_I \lambda_I / 3$. The factor 1.3 was applied to match the extrapolated IR-contribution to the pseudo-bolometric fluxes obtained via direct integration of observed near-IR $JHK$ photometry (see below).

Finally, the bolometric fluxes are corrected for distances using the distance moduli taken from the `SNooPy2` fits (Section 3.1).

This procedure was validated by comparing the estimated UV and IR-contributions to those calculated from existing data for three well-observed normal Type Ia SNe: 2011fe (Brown et al. 2014; Vinkó et al. 2012; Matheson et al. 2012), 2017erp (Brown et al. 2018) and 2018oh (Li et al. 2018). All data were downloaded from the *Open Supernova Catalog*[7] (Guillochon et al. 2017).

Fig. 3 shows the comparison of the $BVRI$-extrapolated pseudo-bolometric fluxes (colored symbols) with the

[7] https://sne.space

**Table 2.** Best-fit parameter from SNooPy2

| Name | $E(B-V)_{MW}$ | $E(B-V)_{host}$ | $T_{max}$ | $\mu_0$ | $s_{BV}$ | $\Delta m_{15}$ | $\chi^2$ |
|---|---|---|---|---|---|---|---|
| | mag | mag | MJD | mag | | mag | |
| SN 2011fe | 0.0075 | 0.048 (0.060) | 55815.31 (0.06) | 29.08 (0.082) | 0.940 (0.031) | 1.175 (0.008) | 1.058 |
| Gaia16alq | 0.0576 | 0.089 (0.061) | 57508.11 (0.14) | 35.05 (0.084) | 1.132 (0.033) | 0.939 (0.024) | 1.358 |
| SN 2016asf | 0.1149 | 0.076 (0.097) | 57464.66 (0.11) | 34.69 (0.083) | 1.001 (0.031) | 1.102 (0.023) | 2.722 |
| SN 2016bln | 0.0249 | 0.213 (0.061) | 57499.40 (0.34) | 34.78 (0.116) | 1.058 (0.032) | 1.005 (0.024) | 3.839 |
| SN 2016coj | 0.0163 | 0.000 (0.061) | 57548.30 (0.34) | 32.08 (0.083) | 0.788 (0.030) | 1.438 (0.020) | 1.954 |
| SN 2016eoa | 0.0633 | 0.242 (0.062) | 57615.66 (0.35) | 34.24 (0.101) | 0.775 (0.032) | 1.486 (0.036) | 1.867 |
| SN 2016ffh | 0.0239 | 0.198 (0.061) | 57630.48 (0.36) | 34.61 (0.094) | 0.926 (0.032) | 1.082 (0.018) | 2.392 |
| SN 2016gcl | 0.0630 | 0.056 (0.061) | 57649.48 (0.36) | 35.45 (0.090) | 1.155 (0.043) | 0.901 (0.031) | 2.792 |
| SN 2016gou | 0.1095 | 0.258 (0.060) | 57666.40 (0.34) | 34.25 (0.104) | 0.984 (0.031) | 0.925 (0.032) | 6.560 |
| SN 2016ixb | 0.0520 | 0.077 (0.061) | 57745.11 (0.37) | 35.620 (0.087) | 0.758 (0.032) | 1.657 (0.039) | 2.072 |
| SN 2017cts | 0.0265 | 0.158 (0.061) | 57856.83 (0.35) | 34.56 (0.088) | 0.931 (0.030) | 1.208 (0.020) | 1.394 |
| SN 2017drh | 0.1090 | 1.396 (0.062) | 57890.94 (0.36) | 32.29 (0.326) | 0.838 (0.031) | 1.352 (0.065) | 2.075 |
| SN 2017erp | 0.0928 | 0.210 (0.061) | 57934.40 (0.35) | 32.34 (0.097) | 1.174 (0.030) | 1.129 (0.011) | 1.627 |
| SN 2017fgc | 0.0294 | 0.162 (0.061) | 57959.77 (0.37) | 32.61 (0.092) | 1.137 (0.037) | 1.086 (0.027) | 1.761 |
| SN 2017fms | 0.0568 | 0.022 (0.061) | 57960.09 (0.35) | 35.52 (0.084) | 0.746 (0.033) | 1.425 (0.026) | 1.875 |
| SN 2017hjy | 0.0768 | 0.211 (0.061) | 58056.02 (0.35) | 34.05 (0.096) | 0.949 (0.031) | 1.137 (0.011) | 1.519 |
| SN 2017igf | 0.0456 | 0.158 (0.061) | 58084.61 (0.36) | 32.80 (0.096) | 0.608 (0.032) | 1.757 (0.006) | 3.461 |
| SN 2018oh | 0.0382 | 0.071 (0.061) | 58162.96 (0.37) | 33.40 (0.083) | 1.089 (0.034) | 0.989 (0.013) | 1.231 |

ones obtained by direct integrations from the UV to the NIR. In the latter case, the integral of a Rayleigh-Jeans tail was also added to the final bolometric flux, but the tail was fit to the $K$-band flux ($f_K$) instead of $f_I$ and the factor 1.3 was not applied.

The top-left panel exhibits the comparison of the flux ratio $f_{BUV}$ to $f_{bol}$ as a function of phase, where $f_{BUV}$ is the integrated flux between the $B$-band and 2000 Å and $f_{bol}$ is the total bolometric flux. The filled circles are based on interpolated fluxes (as described above), while the lines are from direct integration using the UV data from the *Neil Gehrels Swift Observatory* database. It is seen that there is reasonable agreement between the interpolated and the directly integrated blue-UV fluxes. The bottom-left panel shows the same flux ratio computed from the interpolated data but for all SNe in our sample. This illustrate that there is no major difference in the flux ratios between the slow- and fast-decliner SNe Ia around maximum light, despite a $\sim 5$ percent relative flux uncertainty (estimated from the scattering of the data) that we include in the final flux uncertainty estimate.

In the top-right panel the full bolometric LC from direct integration (solid line) and the one based on extrapolation (circles) is shown for the extremely well-observed SN 2011fe. The insets illustrate the same but only for the UV (left) and NIR (right) regimes. Again, there seems to be good agreement between the directly integrated and the extrapolated bolometric fluxes. In the bottom-right panel the calculated luminosity evolution is plotted for all SNe in our sample.

It is concluded that the pseudo-bolometric LCs obtained from extrapolations described above are reliable representations of the true bolometric data, and the systematic errors due to the missing bands do not exceed $\sim 5$ percent. Together with the errors due to uncertainties in the distances (see above), the final relative uncertainty of the bolometric fluxes are estimated as $\sim 10$ percent.

### 3.3. *Fitting the bolometric light curve*

We estimated the physical parameters of the SN ejecta via applying the radiation-diffusion model of Arnett (1982), fitting the bolometric LCs with the `Minim` code (Chatzopoulos et al. 2013). This is a Monte-Carlo code utilizing the Price-algorithm that intends to find the position of the absolute minimum on the $\chi^2$-hypersurface within the allowed volume of the parameter space. Parameter uncertainties are estimated from the final distribution of $N = 200$ test points that probe the parameter space around the $\chi^2$ minimum where $\Delta\chi^2 \leq 1$. See Chatzopoulos et al. (2013) for more details.

The fitted parameters were the following: the time of the first light ($t_0$), the light curve time scale ($t_{lc}$), the gamma-ray leaking time scale ($t_\gamma$), and the initial nickel mass ($M_{Ni}$). These parameters can be found in Table 3. The final uncertainty of the nickel mass also contains the error of the distance (as given by `SNooPy2`) which is added to the fitting uncertainty reported by `Minim` in quadrature. Figure 12 in the Appendix shows the best-fit bolometric LCs corresponding to the smallest $\chi^2$.

The crucial parameter in the semi-analytic LC codes is the effective optical opacity ($\kappa$) that is assumed to be constant both in space and time. To estimate the effective optical opacity for our sample, we applied the same technique as done by Li et al. (2018) for SN 2018oh recently. This technique is based on the combination of the light curve time scale, $t_{lc}$ and that of the gamma-ray leakage, $t_\gamma$. These parameters can be expressed with the physical parameters of the ejecta as follows

$$t_{lc}^2 = \frac{2\kappa M_{ej}}{\beta c v_{exp}} \quad \text{and} \quad t_\gamma^2 = \frac{3\kappa_\gamma M_{ej}}{4\pi v_{exp}^2} \tag{2}$$

where $M_{ej}$ is the ejecta mass, $\beta = 13.8$ is a fixed LC parameter related to the density distribution, $v_{exp}$ is the expansion velocity and $\kappa_\gamma = 0.03$ cm$^2$g$^{-1}$ is the opacity for $\gamma$-rays (Arnett 1982; Clocchiatti & Wheeler 1997; Valenti et al. 2008; Chatzopoulos et al. 2012; Wheeler et al. 2015; Li et al. 2018).

Since $t_{lc}$ and $t_\gamma$ are measured quantities, the two formulae in Equation 2 contains three unknowns: $M_{ej}$, $v_{exp}$, and $\kappa$. Following Li et al. (2018), we apply two additional constraints for $M_{ej}$ and $v_{exp}$ to get upper and lower limits for $\kappa$. Assuming that the ejecta mass cannot exceed the Chandrasekhar limit ($M_{ej} \leq M_{Ch}$) we get a lower limit for the optical opacity, $\kappa^-$, while assuming a lower limit for $v_{exp}$ as $v_{exp} \geq 10,000$ km s$^{-1}$ we get an upper limit, $\kappa^+$ (see Equation 2.).

In the first case the lower limit for $\kappa$ can be calculated as

$$\kappa^- = \sqrt{\frac{3\kappa_\gamma t_{lc}^4 \beta^2 c^2}{16\pi t_\gamma^2 M_{Ch}}}. \tag{3}$$

Second, the lower limit for the expansion velocity, $v_{exp} = 10,000$ km s$^{-1}$, implies

$$\kappa^+ = \frac{3\kappa_\gamma t_{lc}^2 \beta c}{8\pi v_{exp} t_\gamma^2}. \tag{4}$$

The inferred $\kappa$ and $\kappa^+$ values can be found in Table 3.

Finally we estimate $\kappa$ as the average of $\kappa$ and $\kappa^+$, and derive $M_{ej}$ and $v_{exp}$ via the following expressions

$$M_{ej} = \frac{3\kappa_\gamma t_{lc}^4 \beta^2 c^2}{16\pi t_\gamma^2 \kappa^2} \quad \text{and} \quad v_{exp} = \frac{3\kappa_\gamma t_{lc}^2 \beta c}{8\pi\kappa t_\gamma^2}. \tag{5}$$

**Table 3.** Best-fit and inferred parameters from the bolometric LC fitting

| Name | $t_0$ (day) | $t_{lc}$ (day) | $t_\gamma$ (day) | $M_{Ni}$ ($M_\odot$) | $\kappa^-$ ($cm^2g^{-1}$) | $\kappa^+$ ($cm^2g^{-1}$) | $M_{ej}$ ($M_\odot$) | $v_{exp}$ (km $s^{-1}$) | $E_{kin}$ ($10^{51}$ erg) | $\chi^2$ |
|---|---|---|---|---|---|---|---|---|---|---|
| 2011fe | 16.59 (0.061) | 14.87 (0.321) | 37.60 (0.670) | 0.567 (0.042) | 0.166 | 0.232 | 1.002 (0.070) | 11660 (542) | 0.817 (0.407) | 0.517 |
| Gaia16alq | 19.92 (0.418) | 13.78 (0.899) | 46.669 (0.717) | 0.744 (0.055) | 0.115 | 0.129 | 1.274 (0.330) | 10594 (1421) | 0.858 (0.269) | 1.755 |
| 2016asf | 15.08 (2.579) | 11.35 (1.140) | 39.192 (1.329) | 0.597 (0.149) | 0.093 | 0.124 | 1.051 (0.430) | 11459 (2429) | 0.828 (0.491) | 0.502 |
| 2016bln | 17.42 (0.342) | 14.00 (1.219) | 44.508 (1.125) | 0.789 (0.097) | 0.124 | 0.146 | 1.211 (0.430) | 10833 (1964) | 0.852 (0.363) | 0.662 |
| 2016coj | 14.17 (0.261) | 10.57 (0.367) | 32.967 (0.863) | 0.401 (0.053) | 0.095 | 0.152 | 0.856 (0.130) | 12298 (1070) | 0.777 (0.557) | 0.487 |
| 2016eoa | 14.07 (3.053) | 10.55 (1.092) | 39.038 (0.935) | 0.482 (0.103) | 0.080 | 0.108 | 1.047 (0.440) | 11483 (2439) | 0.828 (0.498) | 0.617 |
| 2016ffh | 14.03 (1.16) | 9.736 (0.521) | 40.521 (0.926) | 0.573 (0.078) | 0.067 | 0.088 | 1.035 (0.230) | 11298 (1316) | 0.836 (0.363) | 0.653 |
| 2016gcl | 17.79 (2.184) | 15.85 (1.177) | 43.623 (1.182) | 0.689 (0.164) | 0.162 | 0.195 | 1.185 (0.360) | 10931 (1728) | 0.849 (0.343) | 0.280 |
| 2016gou | 15.03 (0.525) | 11.05 (0.798) | 45.793 (1.412) | 0.678 (0.063) | 0.075 | 0.086 | 1.250 (0.30) | 10696 (1681) | 0.856 (0.304) | 0.263 |
| 2016ixb | 15.64 (2.088) | 13.12 (2.364) | 30.520 (1.345) | 0.483 (0.064) | 0.159 | 0.274 | 0.777 (0.30) | 12653 (3050) | 0.747 (0.539) | 0.177 |
| 2017cts | 14.23 (1.101) | 9.97 (1.259) | 42.485 (0.959) | 0.539 (0.063) | 0.066 | 0.081 | 1.151 (0.58) | 11062 (2838) | 0.845 (0.505) | 0.506 |
| 2017erp | 17.96 (0.092) | 17.40 (0.518) | 37.603 (1.084) | 0.975 (0.083) | 0.227 | 0.317 | 1.002 (0.13) | 11661 (966) | 0.817 (0.414) | 0.413 |
| 2017fgc | 16.21 (0.239) | 12.50 (0.386) | 45.398 (0.941) | 0.692 (0.047) | 0.097 | 0.112 | 1.237 (0.16) | 10734 (799) | 0.855 (0.210) | 0.253 |
| 2017fms | 14.04 (0.504) | 10.58 (0.575) | 34.612 (0.731) | 0.360 (0.029) | 0.091 | 0.138 | 0.909 (0.20) | 12066 (1407) | 0.794 (0.523) | 0.264 |
| 2017hjy | 16.29 (0.492) | 12.83 (0.823) | 39.484 (0.840) | 0.688 (0.057) | 0.117 | 0.156 | 1.060 (0.270) | 11425 (1545) | 0.830 (0.406) | 0.213 |
| 2017igf | 19.58 (0.933) | 15.30 (1.353) | 34.554 (1.193) | 0.420 (0.051) | 0.191 | 0.291 | 0.906 (0.320) | 12070 (2291) | 0.792 (0.572) | 0.779 |
| 2018oh | 14.86 (0.864) | 11.17 (1.098) | 44.654 (0.928) | 0.598 (0.059) | 0.078 | 0.092 | 1.217 (0.480) | 10824 (2175) | 0.856 (0.394) | 0.187 |

Having $M_{ej}$ and $v_{exp}$ evaluated, we express the kinetic energy of ejecta as $E_{kin} = 0.3 \cdot M_{ej} \cdot v_{exp}^2$ (Arnett 1982; Chatzopoulos et al. 2012).

The results of these calculations are collected in Table 3, where the uncertainties (given in parentheses, as previously) are calculated via error propagation taking into account the uncertainties of the fitted timescales and the mean optical opacity, the latter approximated as $\Delta\kappa \approx 0.5(\kappa^+ - \kappa^-)$.

In order to illustrate that the ejecta mass can be inferred from the combination of $t_{lc}$ and $t_\gamma$ via Eq. 5, we constructed model LCs with different ejecta parameters. The left panel of Fig. 4 shows some of them corresponding to $\kappa = 0.1$ $cm^2g^{-1}$, $v_{exp} = 11,000$ km $s^{-1}$, and $M_{ej}$ in between 0.5 and 2.1 $M_\odot$. It can be seen that larger $M_{ej}$ implies both longer rise time and slower decline rate consistently with Eq. 2. The right panel indicates the correlation between the ejecta mass and the two time scale parameters, $t_{lc}$ and $t_\gamma$. Here $t_\gamma$ is plotted with squares while $t_{lc}$ with triangles, and different colors code different physical parameters as follows: blue means $v_{exp} = 11,000$ km $s^{-1}$, $\kappa = 0.1$ $cm^2g^{-1}$, green denotes $v_{exp} = 15,000$ km $s^{-1}$, $\kappa = 0.1$ $cm^2g^{-1}$, and orange is $v_{exp} = 11,000$ km $s^{-1}$, $\kappa = 0.2$ $cm^2g^{-1}$. As it is expected, the shorter the time scales, the lower the model ejecta mass, suggesting that the combination of $t_{lc}$ and $t_\gamma$ outlined above may indeed provide realistic estimates for $M_{ej}$.

We use two SNe as reference objects in order to test the consistency of our LC modeling described above with those presented in other studies. SN 2011fe is chosen as the first test object due to the availability of precise, high-cadence observations spanning from the near-UV to the near-IR regimes (see Section 3.2). Scalzo et al. (2014) modeled the bolometric LC of SN 2011fe and obtained $M_{ej} = 1.19 \pm 0.12$ $M_\odot$ and $M_{Ni} = 0.42 \pm 0.08$ $M_\odot$ for the ejected mass and the nickel mass, respectively. Our best-fit results are $M_{ej} = 1.00 \pm 0.070$ $M_\odot$ and $M_{Ni} = 0.567 \pm 0.042$ $M_\odot$ (see Table 3). It is seen that these two estimates are only marginally consistent: the difference between the two ejecta masses exceeds $1\sigma$ slightly, while the $^{56}Ni$-masses differ by $\sim 2\sigma$. In addition to the sensitivity of the $^{56}Ni$-mass to the uncertainties in the distance, this highlights the possible systematic differences between the two modeling schemes applied by Scalzo et al. (2014) and in this paper: Scalzo et al. (2014) used only the late-time bolometric LC to constrain the ejecta and nickel masses via $t_\gamma$ based on the method of Jeffery (1999), while we fit the full Arnett-model to the entire LC. Note that the $^{56}Ni$ mass of SN 2011fe has also been determined in several other papers, including Pereira et al. (2013) ($0.53 \pm 0.11$ $M_\odot$), Mazzali et al. (2015) ($0.47 \pm 0.07$ $M_\odot$) and Zhang et al. (2016) (0.57 $M_\odot$). The scattering of these various estimates suggest a value of $M_{Ni} \sim 0.5 \pm 0.1$ $M_\odot$ for SN 2011fe, which makes both our result and that of Scalzo et al. (2014) consistent.

On the other hand, good agreement is found between the parameters of the other test object, SN 2018oh. Recently Li et al. (2018) derived $M_{ej} = 1.27 \pm 0.15$ $M_\odot$ and $M_{Ni} = 0.55$ $M_\odot$, which are very similar to our best-fit values (Table 3), $M_{ej} = 1.22 \pm 0.48$ $M_\odot$ and $M_{Ni} = 0.60 \pm 0.06$ $M_\odot$. Even though Li et al. (2018) applied the same method for the LC fitting as we use in

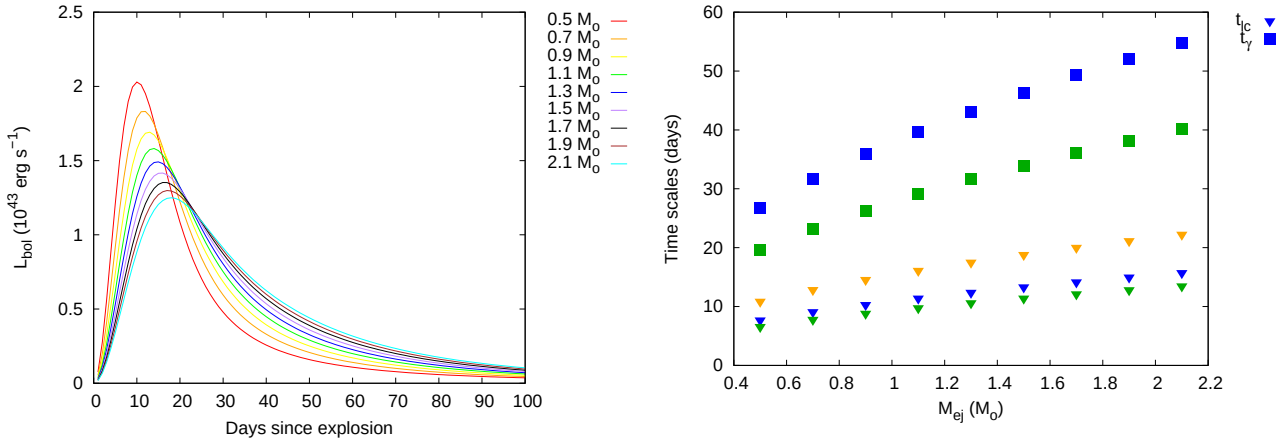


**Figure 4.** Left panel: bolometric LCs for models having $M_{ej}$ in between 0.5 and 2.1 $M_\odot$. All other input parameters for the models were fixed as $R_0 = 0.01 R_\odot$, $v_{exp} = 11\,000$ km s$^{-1}$, $\kappa = 0.1$ cm$^2$g$^{-1}$, and $M_{Ni} = 0.6$ $M_\odot$. Right panel: $t_{lc}$ (triangles) and $t_\gamma$ (squares) as a function of $M_{ej}$. The values corresponding to $v_{exp} = 11000$ km s$^{-1}$ and $\kappa = 0.1$ cm$^2$g$^{-1}$ are plotted with blue, $v_{exp} = 15000$ km s$^{-1}$ and $\kappa = 0.1$ cm$^2$g$^{-1}$ with green, and $v_{exp} = 11000$ km/s, $\kappa = 0.2$ cm$^2$g$^{-1}$ with orange symbols.

this paper, their bolometric LC was assembled from a much denser, more extended dataset, including observed near-UV and near-IR photometry. The good agreement between our best-fit parameters and theirs suggests that our parameters are not unrealistic, and probably do not suffer from severe systematic errors.

## 4. DISCUSSION

### 4.1. *Early color evolution*

In Fig. 5 we plot the early $(B-V)_0$ colors, corrected for both Milky Way and host galaxy reddening (Table 2), of our sample together with the data for several other well-observed SNe Ia: SN 2017cbv (Hosseinzadeh et al. 2017), SN 2011fe (Vinkó et al. 2012), SN 20112cg (Vinkó et al. 2018), SN 2017fr (Contreras et al. 2018), SN 2009ig (Marion et al. 2016; Foley et al. 2012), iPTF16abc (Miller et al. 2018), SN 2012ht (Vinkó et al. 2018) and SN 2013dy (Vinkó et al. 2018)). In the following we investigate the pre-maximum color evolution of our observed sample.

Early-phase $(B-V)_0$ observations of SNe Ia suggest that they can be divided into two categories: early-red and early-blue type (e.g. Stritzinger et al. 2018). The cause of this dichotomy is still debated (see Section 1). For example, Miller et al. (2018) proposed physical models for the progenitor system and the explosion of iPTF16abc. This SN Ia showed blue, nearly constant $(B-V)_0$ color starting from t $\sim$ -10 days, which was thought to be caused by strong $^{56}$Ni-mixing in the ejecta.

SNe Ia experience a dark phase after shock breakout (SB), before the heating from radioactive decay diffuses through the photosphere. The duration of this dark phase depends on how much $^{56}$Ni is mixed into the outer layers of the ejecta. If $^{56}$Ni is confined to the innermost layers, the dark phase lasts for a few days, so that weak mixing leads to redder colors and moderate luminosity rise. On the contrary, strong mixing results in higher luminosities and bluer optical colors. In the latter case the dark phase does not exist or very short, because the $\gamma$-photons originating from the Ni-decay rapidly diffuse out from the ejecta. Shappee et al. (2019) found that strong mixing accounts for the early excess light in the LC of SN 2018oh observed by *Kepler* during the K2-C16 campaign, although its color could not be constrained by the unfiltered K2 observations.

Another possibility for the early blue flux is the collision of the ejecta into a nearby companion star or some kind of a circumstellar envelope. In this case a strong, quickly declining ultraviolet pulse is thought to be the root cause of the excess blue emission during the earliest phases. However, the observability of this emission requires a favorable geometric configuration, i.e. the companion being in front of the SN toward the observer, so it is expected to occur in less than 10% of the actually observed SNe Ia (e.g. Kasen 2010).

With the use of our new photometric data we attempt to investigate the evolution of the early $(B-V)_0$ color for our sample SNe Ia. Fig.5 illustrates that our data are consistent with the colors of other SNe Ia collected from recent literature (plotted as continuous lines in the left panel of Fig. 5) as well as those computed from the Hsiao-template (Hsiao et al. 2007) shown with a black line in both panels. In the latter case the colors are derived by synthetic photometry using Bessell $B$ and $V$

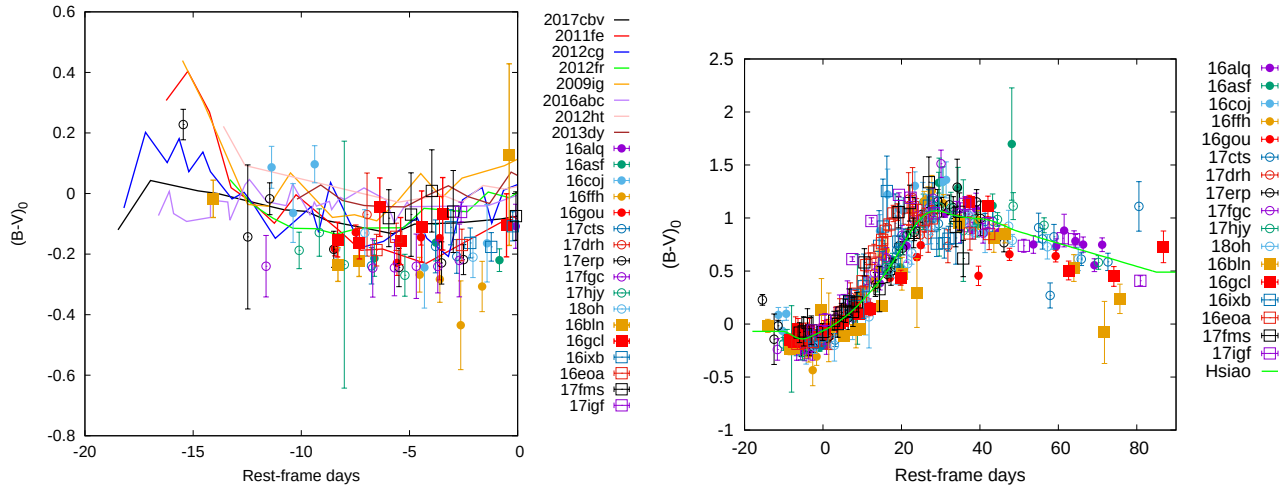


**Figure 5.** The evolution of the reddening-corrected $(B-V)_0$ colors for the sample SNe (colored symbols). Left panel: the pre-maximum color evolution compared to other well-observed SNe collected from literature (colored lines). Right panel: $B-V_0$ colors of the sample plotted together with Hsiao template (green curve) up to 90 days after maximum.

filter functions (Bessell 1990) on the spectral templates of Hsiao et al. (2007).

In order to classify SNe Ia into the early-red and early-blue groups, photometric data taken between −20 and −10 days before maximum is necessary. Between $t = -10$ days and $t_{max}$ the $(B-V)_0$ colors are so similar for most SNe Ia that it is almost impossible to make such a distinction. Unfortunately, most of the SNe Ia in our sample do not have photometry taken early enough for this purpose. During our campaign this very early phase ($-20 < t < -10$ days) have been observed only in two cases: SN 2016bln and 2017erp (see the left panel in Figure 5).

SN 2016bln, a 1991T-like or slow-decliner Ia belonging to the Type SS (Shallow Silicon) subclass on the Branch-diagram (Cenko et al. 2016), shows a very blue early $(B-V)_0$ color in Fig. 5. It suggests that SN 2016bln may be associated with the early-blue group. This is consistent with the findings of Stritzinger et al. (2018) who showed that SNe having early blue colors tend to be located in between the Core Normal and the Shallow Silicon types in the Branch diagram, similar to the 1991T-like events.

On the other hand, SN 2017erp has an early $(B-V)_0$ color that is similar to that of SN 2011fe, thus, it belongs to the early-red group. It is interesting that Brown et al. (2018) showed that SN 2017erp was a near-UV (NUV)-red object, while SN 2011fe was a NUV-blue event. This difference between the NUV-colors seems to be independent from the early-phase optical colors, because 2011fe and 2017erp both had similarly red early $(B-V)_0$ color.

**Table 4.** Parameters of the DDE and PDDE models by Dessart et al. (2014)

| Model | $E_{kin}$ (foe) | $M_{Ni}$ ($M_\odot$) | Model | $E_{kin}$ (foe) | $M_{Ni}$ ($M_\odot$) |
|---|---|---|---|---|---|
| DDC0 | 1.573 | 0.869 | PDDEL1 | 1.398 | 0.758 |
| DDC6 | 1.530 | 0.722 | PDDEL3 | 1.353 | 0.685 |
| DDC10 | 1.520 | 0.623 | PDDEL7 | 1.336 | 0.604 |
| DDC15 | 1.465 | 0.511 | PDDEL4 | 1.344 | 0.529 |
| DDC17 | 1.459 | 0.412 | PDDEL9 | 1.342 | 0.408 |
| DDC20 | 1.442 | 0.300 | PDDEL11 | 1.236 | 0.312 |
| DDC22 | 1.345 | 0.211 | PDDEL12 | 1.262 | 0.268 |
| DDC25 | 1.185 | 0.119 | | | |

This result may suggest that the observed spread in the early NUV- and optical $(B-V)$ colors of SNe Ia has different physical reasons. Brown et al. (2018) concluded that the diversity in the NUV colors is likely due to the metallicity of the progenitor that affects the NUV-continuum and the strength of the Ca H&K features. The fact that SN 2017erp and SN 2011fe have similar early $(B-V)_0$ but different NUV colors may suggest that the early $(B-V)_0$ diversity might not be directly related to the progenitor metallicity.

### 4.2. *Comparison with explosion models*

In this subsection we compare parameters derived from the bolometric LC fitting, in particular the nickel mass, to those taken from several explosion models. First, we consider the DDE and PDDE models computed by Dessart et al. (2014), as listed in Table 4. It is

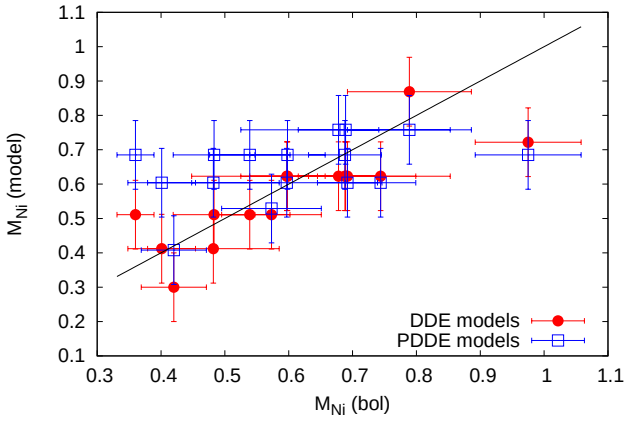


**Figure 6.** Comparison of the Ni-masses derived from the bolometric LCs (plotted on the horizontal axis) with those from DDE (red symbols) and PDDE (blue symbols) models (vertical axis). Solid line represents the expected 1:1 relation.

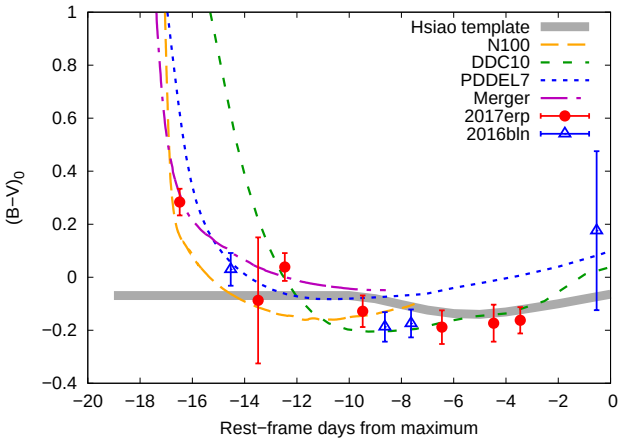


**Figure 7.** Comparison of the early (dereddened) $(B-V)_0$ colors of SN 2017erp (red circles) and 2016bln (blue triangles) with the ones predicted by several Ia explosion models (DDE, PDDE and Violent Merger mechanisms, see text). The color evolution from the empirical Hsiao template is also shown with a thick grey line.

seen that the Ni-masses of these models span the same range than the ones inferred from the bolometric LC fitting (see Table 3), but the kinetic energies of the models are higher by about a factor of $\sim 2$.

PDDE models exhibit strong C II lines shortly after explosion, which are formed in the outer, unburned material. Furthermore, the collision with the previously ejected unbound material surrounding the WD results in the heat-up of the outer layers of the ejecta. Thus, in the PDDE scenario the early color of the SN is bluer, and the luminosity rises faster than in the conventional DDE models.

On the contrary, standard DDE models typically leave no unburned material. Instead, at 1-2 days after explosion they show red optical colors ($(B-V)_0 \sim 1$ mag ), which gets bluer continuously as the SN evolves toward maximum light. After maximum both the DDE and the PDDE scenarios show nearly the same $B-V$ color.

We compare the observed, reddening-corrected $(B-V)_0$ colors of our sample with the predictions from these explosion models. The colors from the models were derived via synthetic photometry applying the standard Bessell $B$ and $V$ filters (Bessell 1990), as above. Note that the in the redshift range of the observed SNe ($z \leq 0.031$) the K-corrections for the $(B-V)$ color indices does not exceed 0.06 mag, which is comparable to the uncertainty of our color measurements in these bands. Thus, the K-corrections were neglected when computing the observed $(B-V)_0$ colors for the comparison with the explosion models. A plot comparing the color curves inferred from DDE and PDDE models with the observed ones can be found in Figures 13 and 14 in the Appendix.

After computing the synthetic $B-V$ curves as a function of phase, the one that has the lowest $\chi^2$ with respect to the observed $(B-V)_0$ color curve was chosen as the most probable explosion model that describes the observed SN. Figure 6 compares the Ni-masses of these models to those derived directly from bolometric LC fitting (Table 3).

Although the grid resolution of the models is inferior, it is seen that the nickel masses from the DDE models nicely correlate with the ones from the bolometric LC fitting (the only outlier, SN 2017erp, may have an overestimated $M_{Ni} \sim 1$ M$_\odot$ due to a reddening issue). The agreement is worse for the PDDE models, where most of the best-fit models have practically the same Ni-mass, $M_{Ni} \sim 0.6$ - $0.7$ M$_\odot$.

In Figure 7 a similar comparison of the synthetic $B-V$ colors from different explosion models with observations is shown, but only for the pre-maximum phases. Beside two models considered above (DDC10 and PDDEL7) by Dessart et al. (2014), synthetic colors from two other theoretical models are also plotted: the N100 explosion model (DDE in a Chandrasekhar-mass WD) by Seitenzahl et al. (2013) and the Violent Merger (VM) model by Pakmor et al. (2012). The color evolution from the empirical Hsiao template (Hsiao et al. 2007) is also shown for comparison.

It is seen that three of these models (N100, PDDEL17 and VM) show similar pre-maximum $B-V$ colors than the observations even at the earliest ($t < -14$ days) phases. The DDC10 model by Dessart et al. (2014) predicts too red $B-V$ color at the earliest phases, while

the colors from the Hsiao template look being too blue. Although the models shown here do not seem to constrain the observed early-blue and early-red events, at least the two SNe in our sample (2016bln and 2017erp) that have been sampled at $t < -14$d have $B-V$ colors consistent with the first three models.

It is concluded that the observed $B-V$ color evolution of SNe Ia seems to be more-or-less reproduced by current models of DDE and/or VM mechanisms. The Ni-masses of the DDE models by Dessart et al. (2014) that match the observed $B-V$ colors are consistent with the Ni-masses inferred from the bolometric LC fitting. This is not true for the PDDE models, as they predict too high nickel masses for SNe that have $M_{Ni} < 0.6$ $M_\odot$ from their bolometric LC fitting.

### 4.3. *Ejecta parameters*

In this section we examine the relations between the inferred ejecta parameters (Table 3) following Scalzo et al. (2014) and Scalzo et al. (2019). Overall, we find similar correlations between the ejecta mass, the Ni-mass and the LC timescales ($t_{cl}$, $t_\gamma$, and $s_{BV}$) to those presented recently by Scalzo et al. (2019).

#### 4.3.1. *Comparison with Scalzo et al. (2014, 2019)*

The top left panel of Figure 8 shows the dependence between the SNooPy2 decline rate parameter $s_{BV}$ and the ejecta mass. Different colors represent different SNe Ia subtypes: normal SNe are plotted with green symbols, while 91T-like events are blue and 91bg-like objects are red.

The dashed line indicates the correlation found by Scalzo et al. (2019) between $M_{ej}$ and $s_{BV}$. It is seen that this correlation is in very good agreement with the observed data. Thus, our results are fully consistent with those of Scalzo et al. (2019). Fitting a straight line to the observed data resulted in the following empirical relation

$$M_{ej} = (1.103\pm0.026) + (0.672\pm0.153)\cdot(s_{BV}-1), \quad (6)$$

which is also plotted in Figure 8 as a continuous line. As seen, this is very close to the relation found by Scalzo et al. (2019).

The top right panel of Figure 8 plots $M_{Ni}$ versus $s_{BV}$. The dashed and continuous lines show the same correlations as found by Scalzo et al. (2019) and this paper, respectively. The latter can be expressed as

$$M_{Ni} = (0.644\pm0.021) + (0.794\pm0.126)\cdot(s_{BV}-1). \quad (7)$$

Equation 7 suggests that 91T-like objects with slower decline rate (i.e. higher $s_{BV}$) tend to have larger Ni-masses, while 91bg-like SNe having lower $s_{BV}$ show smaller $M_{Ni}$.

The bottom left panel in Figure 8 illustrates the dependence between $s_{BV}$ and $t_\gamma$ that is similar to the one found by Scalzo et al. (2014) between their "transparency time scale" and the decline rate parameter. The line represents the fit to the data as

$$t_\gamma = (41.04\pm0.85) + (21.79\pm4.98)\cdot(s_{BV}-1). \quad (8)$$

The correlation between the derived $M_{Ni}$ and $M_{ej}$ masses is shown in the bottom right panel in Figure 8. Except one outlier (SN 2017erp that likely has an overestimated $M_{Ni}$ due to its overestimated reddening), there is a clear correlation between these two inferred parameters, which can be expressed as

$$M_{ej} = (0.992\pm0.184)\cdot M_{Ni} + (0.497\pm109). \quad (9)$$

Scalzo et al. (2019) argued that within the framework of the Arnett-model the ratio of $t_{lc}$ and $t_\gamma$ ($\tau_m/t_0$ in their nomenclature) should be nearly constant, at least for SNe Ia having $M_{ej} < M_{Ch}$, i.e. $t_\gamma \sim t_{lc}$. Figure 9 shows the dependence between our best-fit $t_\gamma$ and $t_{lc}$ values (Table 3) together with the simple linear relation suggested by Scalzo et al. (2019) (plotted as a dashed line). It is seen that the parameters inferred directly from the bolometric LC fitting do not follow the linear trend proposed by Scalzo et al. (2019). Instead, $t_\gamma$ seems to be nearly independent of $t_{lc}$. In fact, this finding agrees with the conclusion by Scalzo et al. (2019) that the ejecta mass can be reliably estimated from $t_\gamma$. It suggests that $t_\gamma$ is a better parameter for getting the ejecta parameters constrained. However, as $t_\gamma$ is more difficult to measure than $t_{lc}$, the combination of the two timescales, as shown in this paper, might be useful to reduce the systematic errors that might occur during the inference of the ejecta parameters solely from a single timescale.

#### 4.3.2. *Comparison with Khatami & Kasen (2018)*

Khatami & Kasen (2018) introduced a new analytic relation between peak time and luminosity. They also inferred a new equation connecting the peak time ($t_{peak}$) of the bolometric LC to the diffusion timescale ($t_d$) of the Arnett-model defined similarly to $t_{lc}$ (see Equation 2). For a centrally located $^{56}$Ni distribution,

$$\frac{t_{peak}}{t_d} = 0.11\cdot\ln(1+\frac{9t_s}{t_d}) + 0.36, \quad (10)$$

where $t_d = (\kappa\cdot M_{ej}/(v\cdot c))^{1/2}$ and $t_s = t_{Ni} = 8.8$ day is the nickel decay time scale.

We can test whether Equation 10 were applicable in the case of our SNe by comparing the best-fit $t_0$ parameter (i.e. the time between the moment of first light and

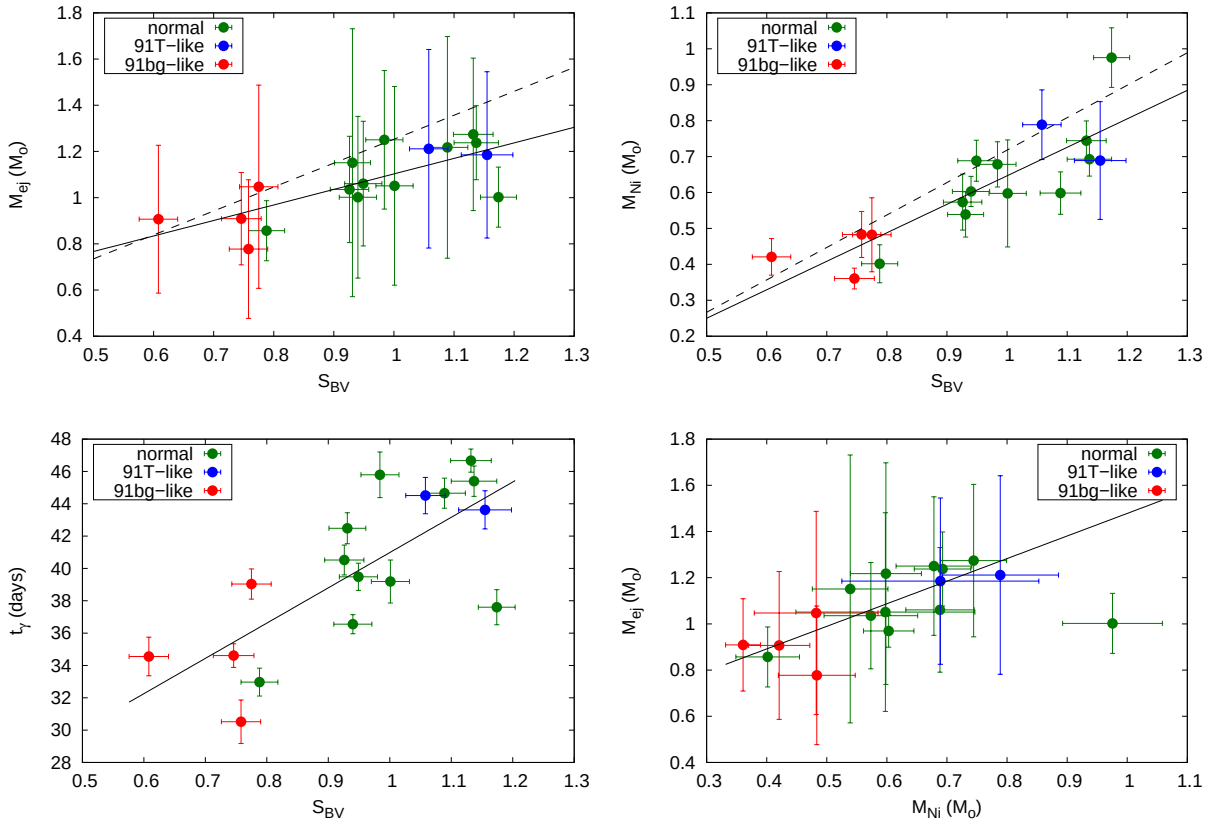


**Figure 8.** Correlation between $s_{BV}$ and $M_{ej}$ (top left panel), $s_{BV}$ and $M_{Ni}$ (top right panel), $s_{BV}$ and $t_\gamma$ (bottom left panel), and $M_{Ni}$ and $M_{ej}$ (bottom right panel). Normal SNe are plotted with green circles, while blue and red circles denote 91T-like and 91bg-like SNe, respectively. Dashed lines in the top panels represent the relations found by Scalzo et al. (2019), while continuous lines indicate fits to the present data.

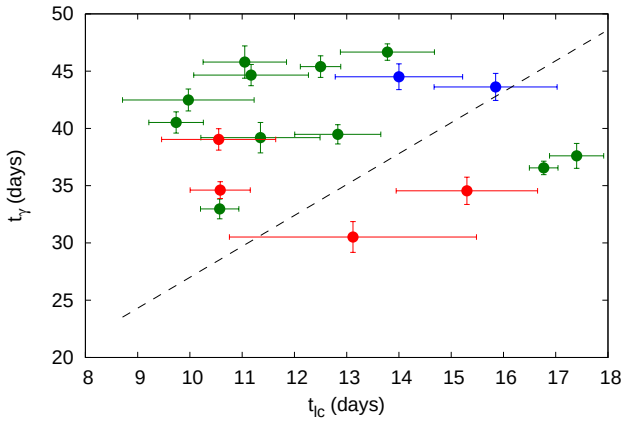


**Figure 9.** The best-fit $t_{lc}$ and $t_\gamma$ values plotted together with the linear relation suggested by Scalzo et al. (2019). Colors have the same meaning as in Fig.8.

the epoch of B-band maximum) from the Arnett-model (Table 3) to the $t_{peak}$ values inferred from Equation 10. The left panel of Figure 10 shows $t_0$ as a function of the corresponding $t_{peak}$ values. The solid line indicates the 1:1 relation, which suggests that the $t_{peak}$ values given by Equation 10 are more-or-less consistent with the best-fit $t_0$ parameters.

Khatami & Kasen (2018) also derived the peak luminosity ($L_{peak}$) as

$$L_{peak} = \frac{2\ \epsilon_{Ni} \cdot M_{Ni} t_s^2}{\beta_K^2 t_{peak}^2}[1-(1+\beta_K t_{peak}/t_s)e^{-\beta_K t_{peak}/t_s}], \quad (11)$$

where $\epsilon_{Ni} = 3.9 \cdot 10^{10} erg\ g^{-1}\ s^{-1}$ is the heating rate of Ni-decay, and $\beta_K$ is the LC parameter introduced by Khatami & Kasen (2018) (not related to the $\beta \sim 13.8$ density distribution parameter in the Arnett-model). Khatami & Kasen (2018) showed that $\beta_K \sim 1$ for a centrally located heating source (i.e. $^{56}$Ni), while mixing the radioactive Ni toward the outer parts of the ejecta tends to increase the value of $\beta_K$.

In the right panel of Figure 10 we plot the nickel masses calculated via Equation 11 using the *observed* $L_{peak}$ values from the assembled bolometric light curves and choosing $\beta_K = 1$, versus the best-fit $M_{Ni}$ parame-

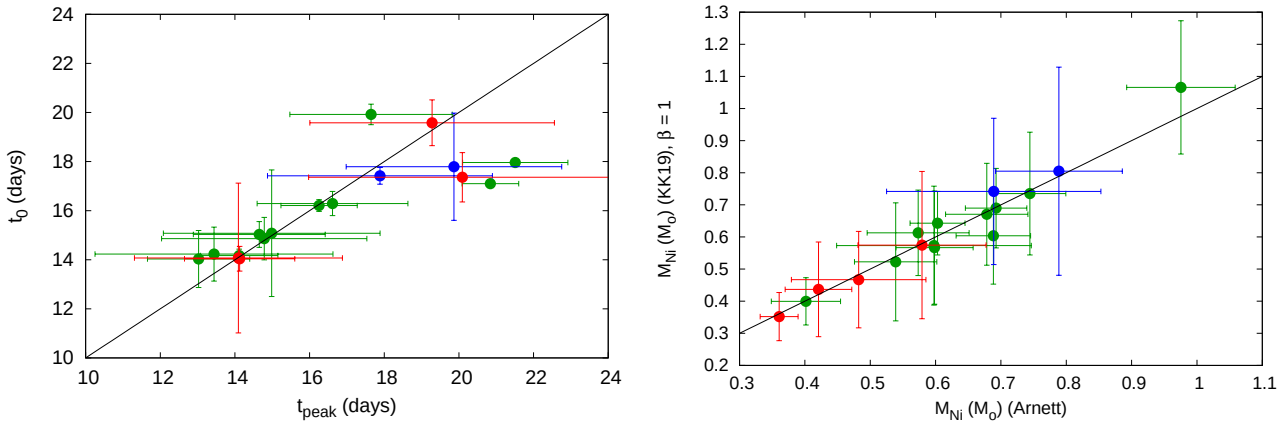


**Figure 10.** Left panel: The LC rise time from the Arnett-model ($t_0$ in Table 3) versus $t_{peak}$ inferred from Equation 10. Right panel: $M_{Ni}$ inferred from Eq. 11. vs. $M_{Ni}$ from the Arnett model. The black line represents the 1:1 relation in both panels. Colors have the same meaning as in Figure 8.

ters from Table 3. It is seen that these two parameters are nicely consistent. Overall, Figure 10 illustrates that the LC timescales and Ni-masses inferred by the bolometric LC fits in this paper are in very good agreement with those resulting from the application of the new theoretical relations given by Khatami & Kasen (2018). This may further strengthen the credibility of using the best-fit parameters from our Arnett-models for representing the real ejecta parameters in the studied SNe Ia.

## 5. SUMMARY

We presented a photometric investigation of 17 Type Ia supernovae observed with the 0.6/0.9 m Schmidt-telescope at Piszkéstető station of Konkoly Observatory, Hungary. The reduced $BVR_CI_C$ LCs were analyzed using the `SNooPy2` public LC-fitter code. The reddening of the host galaxy ($E(B-V)_{host}$), the moment of the B-band maximum light ($T_{max}$), the extinction-free distance modulus ($\mu_0$), and the LC decline rates ($s_{BV}$ and $\Delta m_{15}$) were inferred.

After correcting for the extinction in the Milky Way and the host galaxy, the fluxes of the missing UV- and IR-bands were estimated by extrapolations. The bolometric LCs were constructed applying the trapezodial integration rule, and validated by utilizing the NIR and UV-band data of three well-observed normal Ia SNe, SN 2011fe, SN 2017erp and SN 2018oh. The integrated optical fluxes supplemented by extrapolations into the unobserved UV and IR-bands are found to be reliable representations of the true bolometric data, thus the systematic errors caused by the missing bands should be negligible. Finally, the bolometric fluxes were corrected for distances derived via `SNooPy2`.

We applied the `Minim` code (Chatzopoulos et al. 2012; Li et al. 2018) to fit the bolometric LCs with the radiation diffusion model of Arnett (1982). The optimized parameters of this model were the moment of first light ($t_0$), the LC time scale ($t_{lc}$), the $\gamma$-ray leakage time scale ($t_\gamma$), and the initial nickel-mass ($M_{Ni}$).

One of the critical parameters of the Arnett-model is the value of the optical opacity ($\kappa$), which is approximated as a constant in both space and time. Upper and lower limits for the optical opacity were estimated by using the same method as in Li et al. (2018). This method combines the $t_{lc}$ and $t_\gamma$ parameters, and may give a reliable evaluation of the ejecta mass ($M_{ej}$) and the expansion velocity ($v_{exp}$). As above, comparing the inferred parameters of SN 2011fe and SN 2018oh to those published by Scalzo et al. (2014) and Li et al. (2018), reasonable agreement has been found.

The pre-maximum $(B-V)_0$ color evolution of the sample SNe was also studied in order to decide whether they belong to the early red or early blue group defined recently by Stritzinger et al. (2018). Even though our data are consistent with the expected color evolution of SNe Ia, only two SNe in our sample, SN 2016bln and SN 2017erp, were observed at sufficiently early epochs ($-10$ - $-20$ days before maximum) for this purpose. Based on these early colors, SN 2016bln is classified as a member of the early blue group, which is consistent with its 91T/SS spectral type (Stritzinger et al. 2018). SN 2017erp, NUV-red object (Brown et al. 2018), however, seems to belong to the early red group based on its earliest $(B-V)_0$ color.

The early-phase $(B-V)_0$ colors were also compared to the synthetic colors from Delayed Detonation (DDE), Pulsational Delayed Detonation (PDDE) (Dessart et al. 2014) and other explosion models (e.g. N100 from

Noebauer et al. (2017)) in order to test whether the nickel masses in these models were consistent with those derived from the bolometric LC modeling. We found good agreement between the Ni-masses of DDE models whose color curves match the observed $(B-V)_0$ colors and the Ni-masses inferred from the bolometric LCs. The agreement is worse for the PDDE models, since those models that have synthetic colors most similar to the observed ones have nearly the same Ni-mass, $M_{Ni} \sim 0.65 \pm 0.1$ M$_\odot$.

Finally, we examined the possible correlation between the physical parameters of the ejecta, such as $s_{BV}$ vs $M_{ej}$, $M_{Ni}$, and $t_\gamma$, as well as $M_{ej}$ vs $M_{Ni}$. Similar correlations were found as published recently by Scalzo et al. (2019). Our results also turned out to be consistent with the predictions from the new formalism proposed by Khatami & Kasen (2018).

We express our thanks to an anonymous referee whose criticism and helpful suggestions led to a significant improvement of this paper. This work is part of the project "Transient Astrophysical Objects" GINOP 2.3.2-15-2016-00033 of the National Research, Development and Innovation Office (NKFIH), Hungary, funded by the European Union. This study has also been supported by the Lendület LP2018-7/2018 and the NKFIH K-115709 grants of the Hungarian National Research, Development and Innovation Office, and the Hungarian Academy of Sciences.

## REFERENCES

Arnett, W. D. 1982, ApJ, 253, 785
Astier, P., Guy, J., Regnault, N., et al. 2006, A&A, 447, 31
Bengaly, C. A. P., Jr., Bernui, A., & Alcaniz, J. S. 2015, ApJ, 808, 39
Benitez-Herrera, S., Ishida, E. E. O., Maturi, M., et al. 2013, MNRAS, 436, 854
SExtractor: Software for source extraction, Astronomy & Astrophysics Supplement 317, 393
Bessell, M. S. 1990, PASP, 102, 1181
Bessell, M. S., Castelli, F., & Plez, B. 1998, A&A, 333, 231
Betoule, M., Kessler, R., Guy, J., et al. 2014, A&A, 568, A22
Brimacombe, J., Stone, G., Post, R., et al. 2017, Transient Name Server Discovery Report 2017-391, 1.
Brown, J. 2016, Transient Name Server Discovery Report 2016-644, 1.
Brown, P. J., Breeveld, A. A., Holland, S., Kuin, P., & Pritchard, T. 2014, Ap&SS, 354, 89
Brown, P. J., Hosseinzadeh, G., Jha, S. W., et al. 2018, arXiv:1808.04729
Burns, C. R., Stritzinger, M., Phillips, M. M., et al. 2011, AJ, 141, 19
Burns, C. R., Stritzinger, M., Phillips, M. M., et al. 2014, ApJ, 789, 32
Burns, C. R., Parent, E., Phillips, M. M., et al. 2018, ApJ, 869, 56
Cenko, S. B., Cao, Y., Kasliwal, M., et al. 2016, The Astronomer's Telegram, 8909,
Chatzopoulos, E., Wheeler, J. C., & Vinko, J. 2012, ApJ, 746, 121
Chatzopoulos, E., Wheeler, J. C., Vinko, J., Horvath, Z. L., & Nagy, A. 2013, ApJ, 773, 76
Clocchiatti, A., & Wheeler, J. C. 1997, ApJ, 491, 375
Conley, A., Sullivan, M., Hsiao, E. Y., et al. 2008, ApJ, 681, 482
Conley, A., Guy, J., Sullivan, M., et al. 2011, ApJS, 192, 1
Contreras, C., Phillips, M. M., Burns, C. R., et al. 2018, ApJ, 859, 24
Cruz, I., Holoien, T. W.-S., Stanek, K. Z., et al. 2016, The Astronomer's Telegram, 8784, 1.
Dessart, L., Blondin, S., Hillier, D. J., & Khokhlov, A. 2014, MNRAS, 441, 532
Dimitriadis, G., Foley, R. J., Rest, A., et al. 2019, ApJL, 870, L1
Dhawan, S., Jha, S. W., & Leibundgut, B. 2018, A&A, 609, A72
Dhawan, S., Bulla, M., Goobar, A., et al. 2018, MNRAS, 480, 1445
Fink, M., Röpke, F. K., Hillebrandt, W., et al. 2010, A&A, 514, A53
Foley, R. J., Challis, P. J., Filippenko, A. V., et al. 2012, ApJ, 744, 38
Gagliano, R., Post, R., Weinberg, E., et al. 2016, Transient Name Server Discovery Report 2016-516, 1.
Gagliano, R., Post, R., Weinberg, E., et al. 2017, Transient Name Server Discovery Report 2017-774, 1.
Goldstein, D. A., & Kasen, D. 2018, ApJL, 852, L33
Guillochon, J., Parrent, J., Kelley, L. Z., & Margutti, R. 2017, ApJ, 835, 64
Guy, J., Astier, P., Baumont, S., et al. 2007, A&A, 466, 11
Guy, J., Sullivan, M., Conley, A., et al. 2010, A&A, 523, A7
Hosseinzadeh, G., Sand, D. J., Valenti, S., et al. 2017, ApJL, 845, L11

Hsiao, E. Y., Conley, A., Howell, D. A., et al. 2007, ApJ, 663, 1187
Iben, I., Jr., & Tutukov, A. V. 1984, ApJS, 54, 335
Itagaki, K. 2017, Transient Name Server Discovery Report 2017-647, 1.
Jeffery, D. J. 1999, arXiv e-prints, astro-ph/9907015
Jha, S., Garnavich, P. M., Kirshner, R. P., et al. 1999, ApJS, 125, 73
Jha, S., Riess, A. G., & Kirshner, R. P. 2007, ApJ, 659, 122
Jones, D. O., Riess, A. G., & Scolnic, D. M. 2015, ApJ, 812, 31
Kasen, D. 2010, ApJ, 708, 1025
Kessler, R., Becker, A. C., Cinabro, D., et al. 2009, ApJS, 185, 32
Khatami, D. K., & Kasen, D. N. 2018, arXiv:1812.06522
Khokhlov, A. M. 1991, A&A, 245, 114
Kromer, M., Sim, S. A., Fink, M., et al. 2010, ApJ, 719, 1067
Li, Z., Gonzalez, J. E., Yu, H., Zhu, Z.-H., & Alcaniz, J. S. 2016, PhRvD, 93, 043014
Li, W., Wang, X., Vinkó, J. et al. 2018 ApJ, submitted
Maoz, D., Mannucci, F., & Nelemans, G. 2014, ARA&A, 52, 107
Marion, G. H., Brown, P. J., Vinkó, J., et al. 2016, ApJ, 820, 92
Matheson, T., Joyce, R. R., Allen, L. E., et al. 2012, ApJ, 754, 19
Mazzali, P. A., Sullivan, M., Filippenko, A. V., et al. 2015, MNRAS, 450, 2631
Miller, A. A., Cao, Y., Piro, A. L., et al. 2018, ApJ, 852, 100
Miller, A. A., Laher, R., Masci, F., et al. 2016, The Astronomer's Telegram, 8907, 1.
Noebauer, U. M., Kromer, M., Taubenberger, S., et al. 2017, MNRAS, 472, 2787
Nomoto, K., Thielemann, F.-K., & Yokoi, K. 1984, ApJ, 286, 644
Pakmor, R., Kromer, M., Taubenberger, S., et al. 2012, ApJL, 747, L10
Papadogiannakis, S., Dhawan, S., Morosin, R., et al. 2019, MNRAS, 485, 2343
Pereira, R., Thomas, R. C., Aldering, G., et al. 2013, A&A, 554, A27
Perlmutter, S., Aldering, G., Goldhaber, G., et al. 1999, ApJ, 517, 565
Phillips, M. M. 1993, ApJL, 413, L105
Piascik, A. S., & Steele, I. A. 2016, The Astronomer's Telegram, 8991, 1.
Prieto, J. L., Rest, A., & Suntzeff, N. B. 2006, ApJ, 647, 501
Pskovskii, I. P. 1977, AZh, 54, 1188
Rest, A., Scolnic, D., Foley, R. J., et al. 2014, ApJ, 795, 44
Riess, A. G., Filippenko, A. V., Challis, P., et al. 1998, AJ, 116, 1009
Riess, A. G., Macri, L., Casertano, S., et al. 2012, ApJ, 752, 76
Riess, A. G., Macri, L. M., Hoffmann, S. L., et al. 2016, ApJ, 826, 56
Riess, A. G., Strolger, L.-G., Casertano, S., et al. 2007, ApJ, 659, 98
Sand, D. J., Valenti, S., Tartaglia, L., et al. 2017, The Astronomer's Telegram, 10569, 1.
Scalzo, R., Aldering, G., Antilogus, P., et al. 2014, MNRAS, 440, 1498
Scalzo, R. A., Parent, E., Burns, C., et al. 2019, MNRAS, 483, 628
Scolnic, D., Rest, A., Riess, A., et al. 2014, ApJ, 795, 45
Seitenzahl, I. R., Ciaraldi-Schoolmann, F., Röpke, F. K., et al. 2013, MNRAS, 429, 1156
Shappee, B. J., Holoien, T. W.-S., Drout, M. R., et al. 2019, ApJ, 870, 13
Sim, S. A., Röpke, F. K., Hillebrandt, W., et al. 2010, ApJL, 714, L52
Sim, S. A., Fink, M., Kromer, M., et al. 2012, MNRAS, 420, 3003
Stanek, K. Z. 2016, Transient Name Server Discovery Report 2016-1049, 1
Stanek, K. Z. 2017, Transient Name Server Discovery Report 2017-1273, 1.
Stanek, K. Z. 2018, Transient Name Server Discovery Report 2018-150, 1.
Stritzinger, M., Leibundgut, B., Walch, S., et al. 2006, A&A, 450, 241
Stritzinger, M. D., Shappee, B. J., Piro, A. L., et al. 2018, arXiv:1807.07576
Tonry, J., Denneau, L., Stalder, B., et al. 2016, Transient Name Server Discovery Report 2016-583, 1.
Tonry, J., Denneau, L., Stalder, B., et al. 2016, Transient Name Server Discovery Report 2016-718, 1.
Tonry, J., Stalder, B., Denneau, L., et al. 2017, Transient Name Server Discovery Report 2017-1123, 1.
Valenti, S., Benetti, S., Cappellaro, E., et al. 2008, MNRAS, 383, 1485
Valenti, S., Sand, D. J., & Tartaglia, L. 2017, Transient Name Server Discovery Report 2017-513, 1.
van Rossum, D. R., Kashyap, R., Fisher, R., et al. 2016, ApJ, 827, 128
Vinkó, J., Sárneczky, K., Takáts, K., et al. 2012, A&A, 546, A12

Vinkó, J., Ordasi, A., Szalai, T., et al. 2018, PASP, 130, 064101
Wang, X., Wang, L., Filippenko, A. V., et al. 2013, Science, 340, 170
Wheeler, J. C., Johnson, V., & Clocchiatti, A. 2015, MNRAS, 450, 1295
Whelan, J., & Iben, I., Jr. 1973, ApJ, 186, 1007
Wilk, K. D., Hillier, D. J., & Dessart, L. 2018, MNRAS, 474, 3187
Wood-Vasey, W. M., Miknaitis, G., Stubbs, C. W., et al. 2007, ApJ, 666, 694
Woosley, S. E., & Weaver, T. A. 1994, ApJ, 423, 371
Zhang, K., Wang, X., Zhang, J., et al. 2016, ApJ, 820, 67
Zhang, B. R., Childress, M. J., Davis, T. M., et al. 2017, MNRAS, 471, 2254
Zheng, W., Filippenko, A. V., Mauerhan, J., et al. 2017, ApJ, 841, 64.

## 6. APPENDIX

In the following we present plots of the best-fit `SNooPy2` templates to the multi-color data of our SN sample (Figure 11), the best-fit Arnett-models to the assembled bolometric LCs (Figure 12) and the comparison between the dereddened $(B-V)_0$ color curves and the synthetic colors computed from the DDE and PDDE models by Dessart et al. (2014) (Figures 13 and 14).

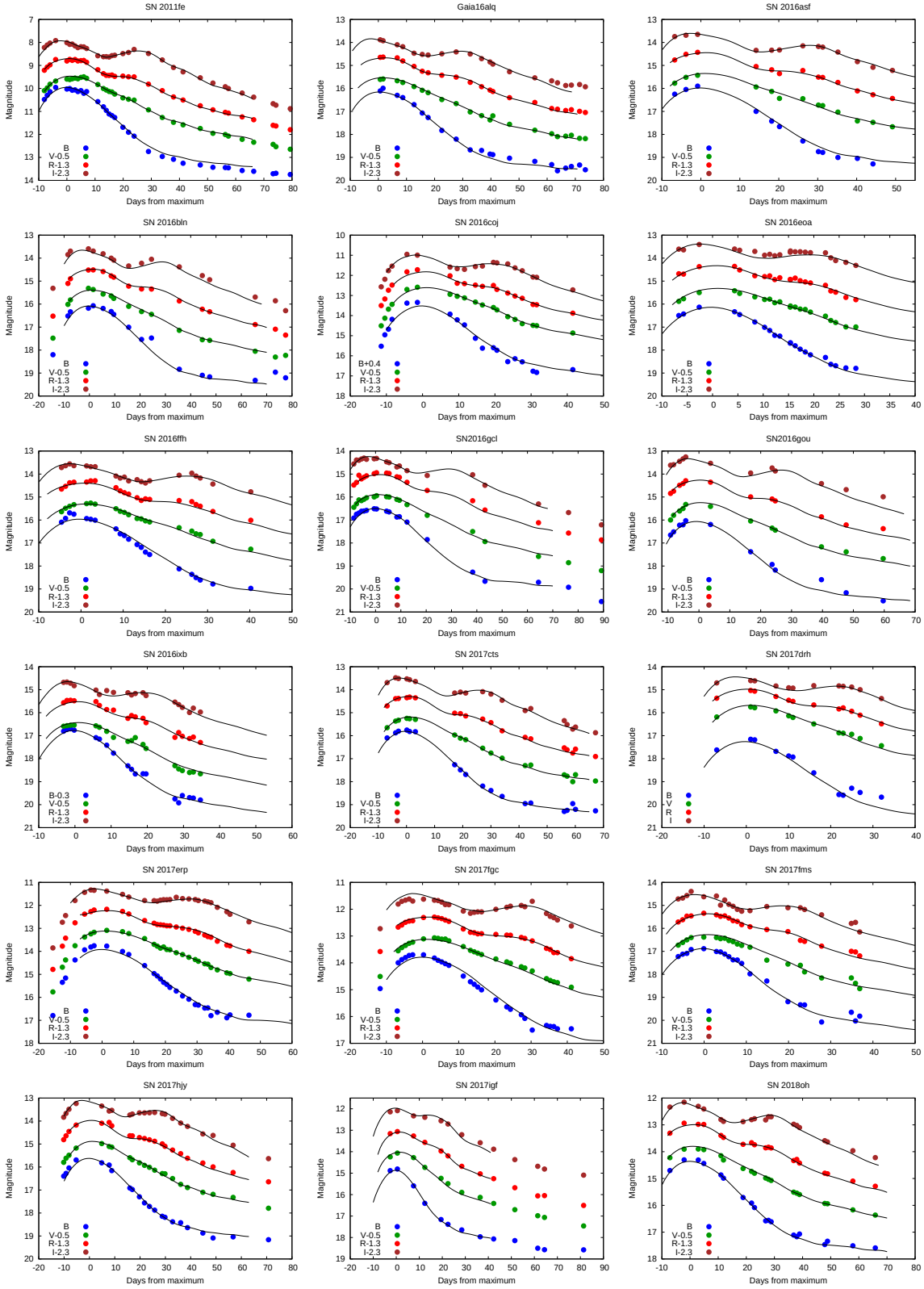


**Figure 11.** BVRI LC-fitting with `SNooPy2`. The curves corresponding to different filters are shifted vertically for better visibility.

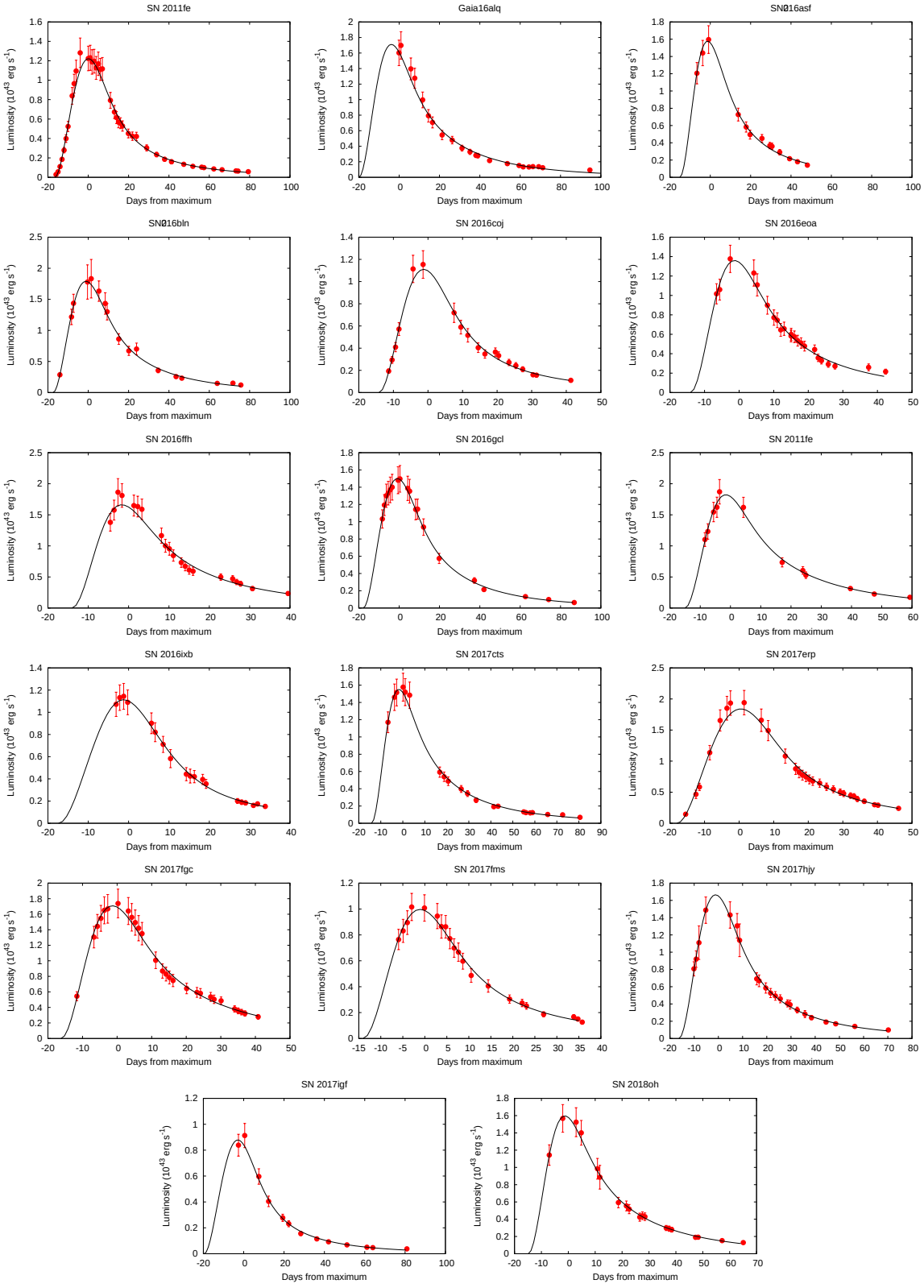


**Figure 12.** The best-fit bolometric LC-s computed with `Minim`.

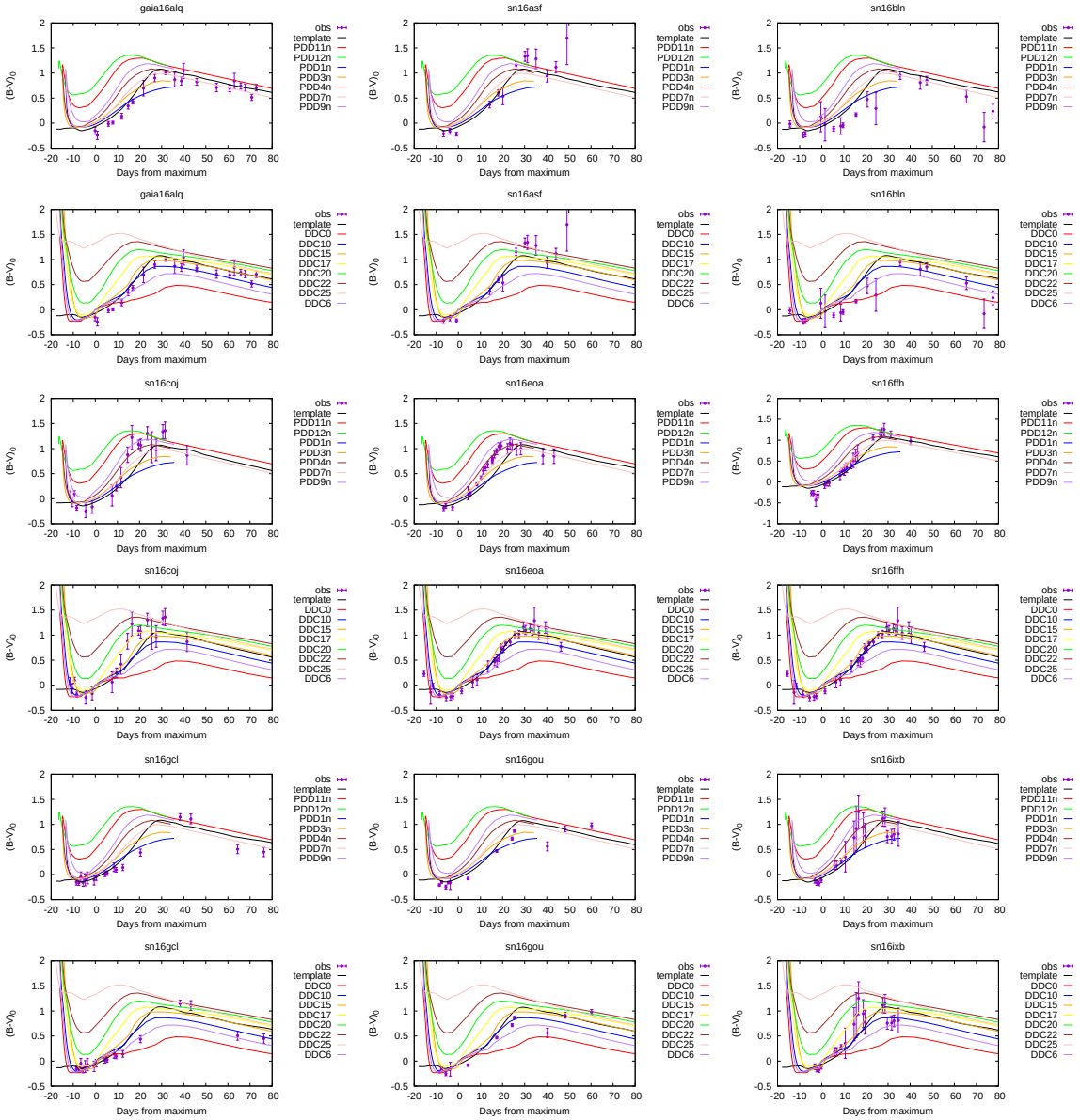


**Figure 13.** Comparison of the observed, de-reddened $(B-V)_0$ colors (filled symbols) with synthetic colors from DDE and PDDE models by Dessart et al. (2014) (colored curves). The black curve corresponds to the synthetic colors inferred from the empirical Hsiao-template (Hsiao et al. 2007).

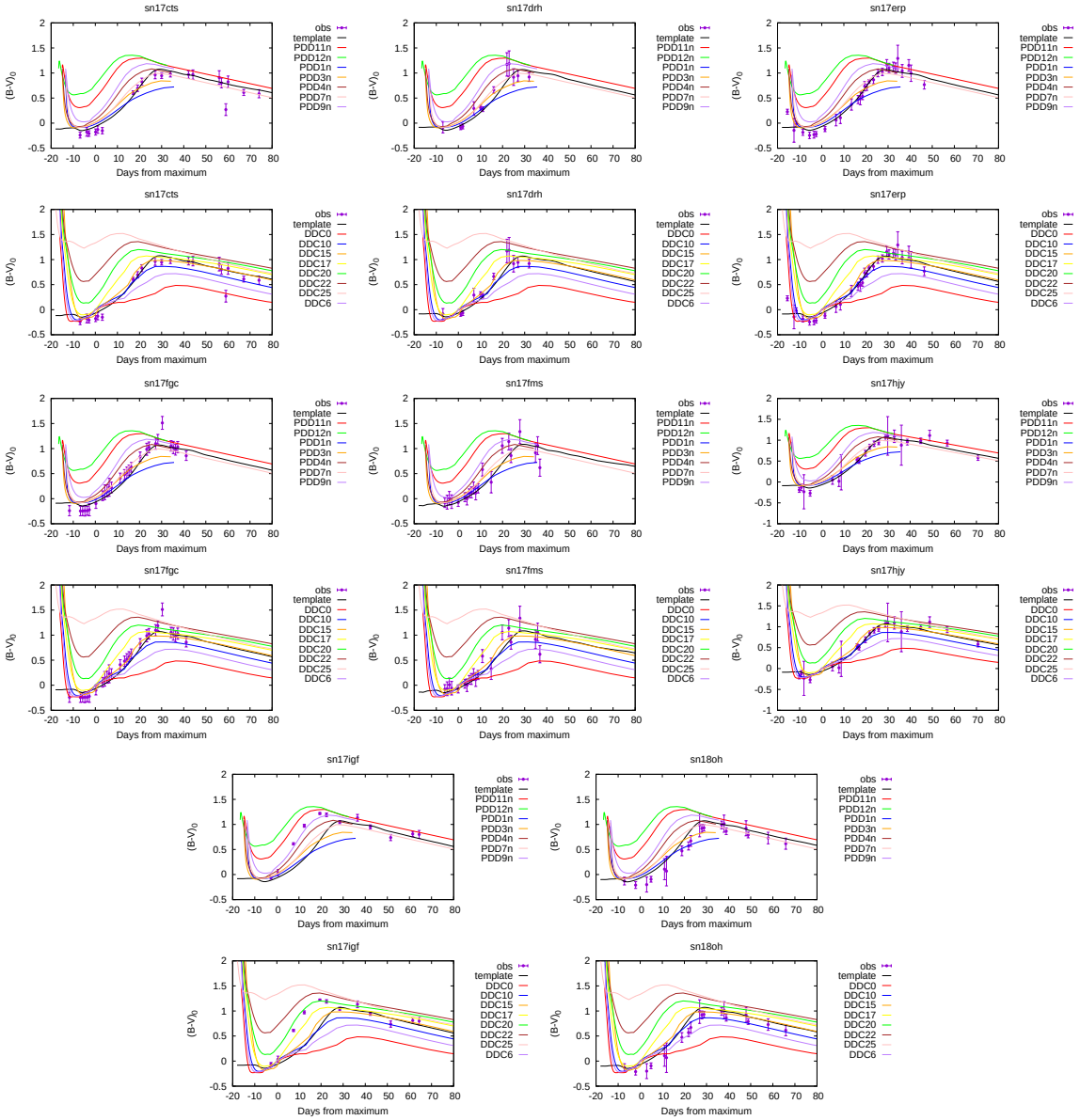


**Figure 14.** The same as Fig.13 but for additional SNe.